



**Australian Government**  
**Department of Defence**  
Defence Science and  
Technology Organisation

# Constitutive Modelling of the Shock Behaviour of a Highly Porous Material

*A. D. Resnyansky*

**Weapons Systems Division**  
Defence Science and Technology Organisation

DSTO-TR-2026

## ABSTRACT

The report studies the constitutive behaviour of highly porous materials. This study is driven by efforts for the development and validation of a multi-phase modelling capability in DSTO, which aims at an enhanced evaluation of blast mitigation by porous materials. A two-phase model is employed for the description of a porous material, for which experimental shock velocity data are widely available in literature. The method deriving Hugoniots from the shock velocity data is critically approached. The importance of the non-equilibrium behaviour analysis is demonstrated, and it is shown that the stress or velocity profiles need to be considered, using relevant experiments and constitutive modelling. It is argued that the apparent anomalous behaviour of the Hugoniots of a highly porous material might be caused by misinterpretation of the experimental data.

## RELEASE LIMITATION

*Approved for public release*

*Published by*

*Weapons Systems Division  
DSTO Defence Science and Technology Organisation  
PO Box 1500  
Edinburgh South Australia 5111 Australia*

*Telephone: (08) 8259 5555  
Fax: (08) 8259 6567*

*© Commonwealth of Australia 2008*

*AR-013-957  
July 2007*

**APPROVED FOR PUBLIC RELEASE**

# Constitutive Modelling of the Shock Behaviour of a Highly Porous Material

## Executive Summary

Porous materials have been used for blast and shock mitigation for a long time. A variety of porous materials such as sand, soil, and concrete are employed as countermeasures to Improvised Explosive Devices (IED) and in a range of activities related to mitigation of the blast and shock due to the explosion of IEDs, landmines, submerged mines and munitions in storage.

Accurate characterisation of materials is important for establishing modelling capabilities. Some porous materials have been characterised extensively in numerous laboratory and underground nuclear tests, mainly in the USA and the USSR. The test results were used for the characterisation of a wide range of porous materials that might be used under extreme pressures in explosive devices and in the high velocity impact environment. Such characterisation was mainly employed for the determination of Hugoniots (curves connecting the material states in front and behind the shock front); in turn, the Hugoniots were used to derive enhanced equations of state. The Hugoniots were obtained with the impedance mismatch method. Hugoniots are sometimes the only data available for derivation of the equations of state that allow hydrocode modelling and evaluation of the material state at high pressures. The data used for the derivation of the Hugoniots are mainly the shock velocities in a tabulated (standard) material and in a material under investigation. Porous materials at extreme pressures exhibit fairly conventional behaviour of the Hugoniots. However, at moderate pressures of the order of several GPa the derived Hugoniots for highly porous materials show an anomalous behaviour resulting in a pressure increase with a decrease of density. A physical explanation was suggested for this abnormality, which necessitated temperature sensitive effects during compression of the material. However, experimental observations of shock profiles in porous materials demonstrate that the shock deformation may occur in several stages, thus, reducing the thermal contribution into the energy absorbed by the material. Although the thermal contribution might be overestimated, the nature of the apparent abnormality of the Hugoniot has not yet been completely explained.

The present report describes the behaviour of a highly porous material at shock compression using a constitutive two-phase model. Conventional equations of state are employed for the material components, which have no abnormalities. The present modelling enables a good description of available shock velocity experimental data for a highly porous copper. The present work has shown that experimental data on stress profiles and constitutive analysis of the behaviour of porous materials are necessary for the material characterisation and evaluation of the material response to blast and shock.

## Authors

### **A.D. Resnyansky** Weapons Systems Division

*Anatoly Resnyansky obtained a MSc in Applied Mathematics and Mechanics from Novosibirsk State University (Russia) in 1979. In 1979-1995 he worked in the Lavrentyev Institute of Hydrodynamics (Russian Academy of Science) in the area of constitutive modelling for problems of high-velocity impact. Anatoly obtained a PhD in Physics and Mathematics from the Institute of Hydrodynamics in 1985. In 1996-1998 he worked in a private industry in Australia. He joined the Weapons Effects Group of the Weapons Systems Division (DSTO) in 1998. His current research interests include constitutive modelling and material characterisation at the high strain rates, ballistic testing and simulation, and theoretical and experimental analysis of the warhead processes. He has more than seventy papers published internationally in this area.*

---

## Contents

1. INTRODUCTION .....	1
2. INTRODUCTION TO THE EXPERIMENTAL METHOD.....	3
3. CONSTITUTIVE MODEL.....	6
4. CONSTITUTIVE RELATIONS FOR POROUS COPPER .....	8
5. MODELLING OF THE SHOCK BEHAVIOUR OF POROUS COPPER .....	12
6. BRIEF DESCRIPTION OF AVAILABLE EXPERIMENTS .....	19
7. RESULTS OF MODELLING THE SHOCK COMPRESSION TESTS .....	21
8. DISCUSSION ON THE NON-EQUILIBRIUM AND ENERGY EXCHANGE KINETICS .....	25
9. CONCLUSIONS .....	30
10. REFERENCES.....	31
APPENDIX A: NONLINEAR RIEMANN PROBLEM FOR ARBITRARY EQUATION OF STATE .....	35
APPENDIX B: IMPEDANCE MISMATCH PROCEDURE.....	37

## 1. Introduction

The characterisation of porous materials has attracted the attention of researchers because of the possibility of expanding the range of state parameters into the high-temperature region. Testing at extreme pressures was possible during the extensive underground nuclear testing programs in the United States and the former Soviet Union in the 1950s. In particular, researchers from the Russian Federal Nuclear Centre (RFNC) of Arzamas, (former Sarov, Nizhniy Novgorod region) reached the Terapascal range of pressures using test assemblies embedded in the rock surrounding a detonating nuclear device [1]. The researchers tested various solid and porous metals and organic compounds. Some of the tests were also carried out in laboratory conditions in the Gigapascal range of pressures, using high explosive (HE) planar and spherical wave generators. To achieve simplicity in experimental set-up the researchers used the Impedance Mismatch (IM) method (see [2]; this method is named the reflection method [3] in the Russian literature). The tests allowed researchers to measure shock wave velocities in a standard and in a material under investigation simultaneously. When having IM-processed the data, the researchers inferred pressure and density in a tested material behind a given shock wave. This enabled them to draw both a Hugoniot of the tested material in the pressure-density space and a line in the shock velocity-particle velocity coordinates, which is frequently also called a Hugoniot. Such the data have been derived for a large number of metals and porous substances (see, for example, [2, 4, 5]). Data for porous copper, which are of specific interest to the present work, have been reported in [6-21]. The present work focuses on an analysis of data for porous copper with an initial density  $\rho_{00}$  that is approximately a quarter of the solid copper density  $\rho_0$  (the porosity  $m = \rho_0 / \rho_{00} = 4$ ). Data relevant to this porosity were reported in [6-12]. Only a few data points for this material have been found in US literature sources [11-12]. Thus, the RFNC Russian team has published the majority of the data, and the majority of the experimental points obtained in laboratory studies have been reported in paper [6]. This data attracts significant attention from modellers because, i) it is quite typical of this class of data for the family of porous materials; and ii) it is a sound representative, the IM-processing of which results in the anomalous feature of the Hugoniot (increase of pressure with a decrease of density). These Hugoniots were used as reference curves for derivation of a large variety of Equations Of State (EOSs), which invoke rather complex high temperature excitation mechanisms in order to describe the abnormality [8, 9, 21] occurring in the pressure range below 50 GPa. It should be mentioned, however, that a paper [22] points out that the necessity of considering some high-temperature mechanisms might be overestimated, when designing EOSs in the pressure range below hundreds of GPa. The test set-up used in publications [6-12] enabled the researchers to draw so-called (D-D)-dependencies that link the shock velocity in a tested material with the shock velocity in a standard material at the same loading conditions. Several examples of such (D-D)-graphs were drawn in [7]. Unfortunately, these dependencies were not detailed in a table form, so an accurate (D-D)-data cannot be recovered from the paper. Even in publications where some isolated (D-D)-points can be found (e.g., [17]) the authors report on a reduced (IM-processed) data using 'a calculated law of attenuation of shock waves', which does not allow the experimental conditions and the test records to be recovered with confidence. From the (D-D)-dependencies, the (P- $\rho$ )- and (D-U)-Hugoniots (here P is pressure,  $\rho$  – density, and U – velocity behind the shock front) have been derived with the IM-technique. The former (P- $\rho$ )-dependence is the Hugoniot actually sought and the (D-U)-line is usually called a Hugoniot as

well. Using these dependencies, EOSs are derived by invoking various physical mechanisms of the material response to compression. One serious simplification, when using the IM-technique, is the jump approximation for a shock wave in porous material. This approximation is accurate enough in solid metals loaded by strong shock waves; however, even metals subject to moderate shock waves exhibit non-equilibrium behaviour. Porous materials exhibit kinetic response that is caused both by a compression precursor and by non-equilibrium (kinetic) behaviour of the main shock wave. Therefore, a complete temporal record of stress or velocity could give proper appreciation of the state achieved during shock loading. However, such experimental information is not readily available and is reported for quite a limited range of porous materials and for limited porosity and load ranges (see, for example, [14-16, 23-24]).

The publications of the RFNC scientists on the shock compression experiments do not provide detailed information, such as an exact set-up description, parameters of the test assemblies and unprocessed recorded shock velocities for standard and tested materials. Instead, the publications deliver post-processed Hugoniots in  $(P-\rho)$ - and  $(D-U)$ -coordinates, which have somehow been corrected in order to take into account various factors such as the shock wave attenuation during its propagation in the experimental set-up (for example, the attenuation correction law mentioned above), non-planarity of impact, curvature of the shock front, etc. The lack of specifications in these set-up descriptions and in the reported results was noted by Nellis et al in [22]. However, even recent publications [1, 4, 25-27] aimed at an extensive description of the test conditions and set-ups of the laboratory experiments from [6-12] also do not give complete details; this issue will be discussed in Section 2.

The present work employs a two-phase constitutive model described elsewhere [24] and briefly outlined in Section 3. This model utilizes conventional equations of state for gaseous and solid phases of a porous material. The present work attempts to estimate experimental set-ups as closely as possible to original ones from the available published information for the tests on the porous ( $m = 4$ ) copper and to simulate the data [6-12] using the constitutive model [24]. The numerical results describe the experimental velocity data (the  $(D-D)$ - and  $(D-U)$ -dependencies) quite well. In doing so, however, the Hugoniots in  $(P-\rho)$ -coordinates obtained from the simulated  $(D-D)$ -results by the IM-processing exhibit no abnormalities. It has been shown that a possible reason for the apparent Hugoniot abnormality is likely to be the use of the jump-like (equilibrium) approximation for the analysis of the shock compression of the porous material. Nevertheless, a kinetic description allowing for an abnormality may also be possible. In that case the abnormality is achieved, when modelling, via suppression of heat exchange from the solid phase; this requires a switch of the heat exchange mechanisms resulting in a pronounced constitutive behaviour and in a significant non-equilibrium behind the shock front. Thus, the present approach demonstrates that the constitutive behaviour of shock waves in a porous material could be an essential factor contributing to the data interpretation. Therefore, experimental data tracing complete stress or velocity profiles, such as those from [14-16, 23-24] would be of great assistance in the evaluation of material shock response. Earlier, attention was also drawn in [28] to the importance of data illustrating constitutive behaviour of porous substances.

## 2. Introduction to the experimental method

The Impedance Mismatch (IM) method is based on derivation of a Hugoniot from the mass, momentum and energy conservation laws balanced across the shock jump:

$$\begin{aligned} \rho \cdot (D - U) &= \rho_0 \cdot D , \\ P &= \rho_0 \cdot D \cdot U , \\ E - E_0 &= \frac{1}{2} P \cdot (1/\rho_0 - 1/\rho) , \end{aligned} \quad (1)$$

where, using an Equation Of State (EOS) in the caloric form  $E = E(\rho, P)$ , the Hugoniot or Rankine-Hugoniot curve  $P_H = P_H(\rho)$  can be obtained from (1). By an inverse procedure the EOS can be found as soon as the Hugoniot is known. In (1) the initial pressure and velocity are assumed to be negligible,  $P$ ,  $\rho$ ,  $U$ ,  $E$  are pressure, density, velocity and internal energy behind the shock front,  $E_0$  and  $\rho_0$  are internal energy and density in front of the shock wave.

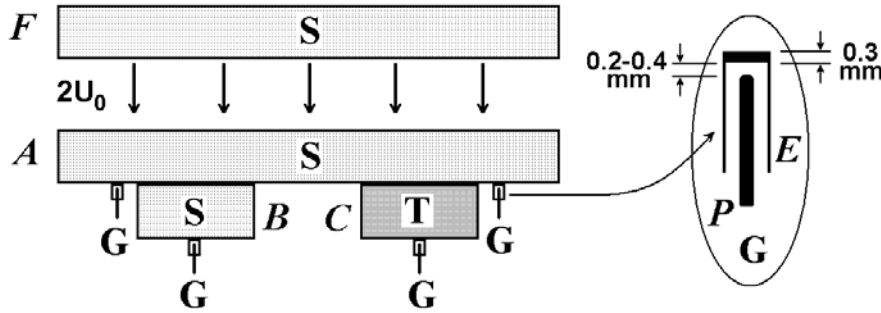


Fig. 1 Schematic of the experimental set-up employed for evaluation of the material shock response

A typical shock response experiment records the shock wave velocity  $D$ . The simplest set-up comprises a screen made from a standard material that has well-known properties and a sample of a material under investigation. Referring to Figure 1 for the set-up, a flyer plate ( $F$ ) with a velocity of  $2U_0$  made from a standard material ( $S$ ) impacts the target assembly consisting a screen ( $A$ ) made from the same material. The screen separates the flyer plate from samples ( $B$ ) and ( $C$ ) made from the material  $S$  and a tested material  $T$ , which are positioned in parallel. The samples are equipped with time of arrival gauges ( $G$ ). In Fig. 1, one of possible configurations of 'electro-contact' gauges used in [6-10] is expanded, showing the details reported in [21, 26] (a similar description can be found in [19]; the gap may approach 1 mm as described in [7]). In these publications, the accuracy of the technique for measurement of the shock wave velocity in solid materials is claimed to be within 1-1.5%. A detailed description of the pin technique has been reported in [29, 30], including a discussion on potential issues and the sources of possible errors. In particular, the paper [29] is more cautious about the technique accuracy and it reports data with accuracy not worse than 5% for shock velocity measurements in condensed materials.

The active element of the gauge (pin  $P$ ) in Fig. 1 is protected by a cup  $E$  against air shock that emerges when free surface of the screen  $A$  or samples  $B$  and  $C$  moves, following the shock wave reflection from the free surface. When the top wall section of the cup  $E$  (the protector that will be referred to below as  $E$  as well) has made contact with the pin it transmits a signal to an oscilloscope. We denote thicknesses of the plates  $F$  and  $A$  to be  $W_f$  and  $W_a$ , and thickness of the samples  $B$  and  $C$  to be  $W_s$ . For the gauge  $G$  we denote thickness of the protector  $E$  to be  $W_b$  (0.3 mm in Fig. 1) and the gap width to be  $W_g$  (0.2-0.4 mm in Fig. 1). An experiment with this set-up determines the shock velocities  $D_s$  and  $D_p$  in the standard and tested materials at approximately the same conditions of loading (when the shock wave starts propagating into the samples  $B$  and  $C$ ), since both samples are placed on the screen  $A$  (made from the standard material  $S$ ).

Below we illustrate how pressure  $P_0$  and material velocity  $U_0$  behind the shock front in the screen can be calculated as an intersection point of a Hugoniot and the Rayleigh line, providing the Hugoniot of the standard material is known and the shock velocity  $D_s$  in this material (sample  $B$ ) has been measured.

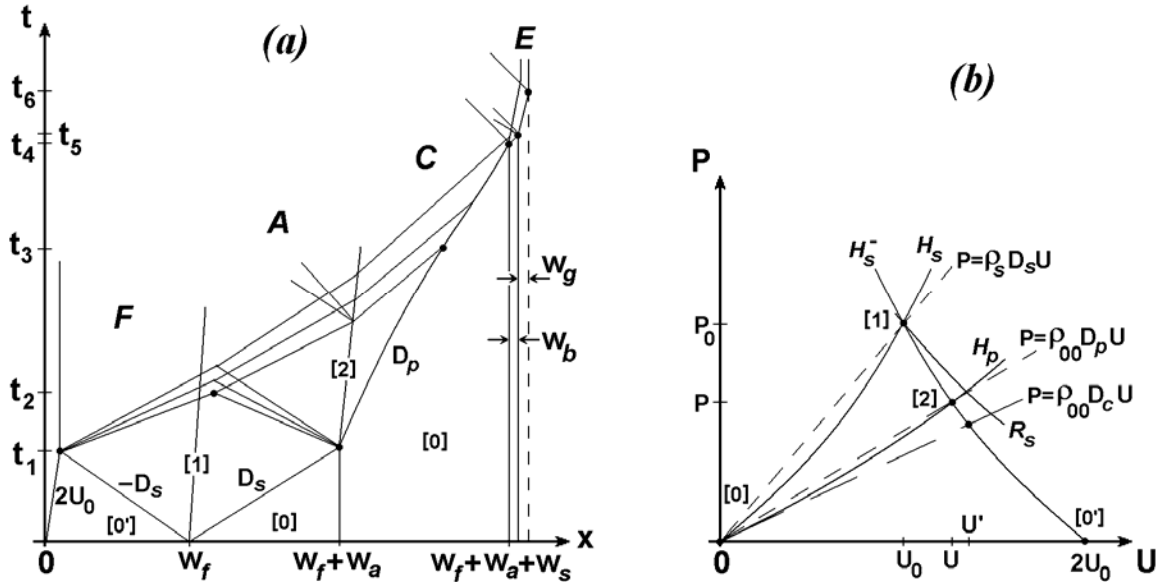


Fig. 2. The shock propagation ( $x$ - $t$ )-diagram for the experimental set-up (a), and the shock adiabat diagram of the shock interaction process (b).

Close examination of the process of interaction of shock waves with the samples shown in Fig. 2, shows that after impact of the flyer plate  $F$  against the screen  $A$ , two shock waves with the same velocity  $D_s$  go left and right into  $F$  and  $A$ , originating from the contact surface ( $x = W_f$ ). Following up the collision event and propagation of the right-going wave through the screen, the wave comes first to the screen-sample interface ( $A$ - $C$ ) and then it breaks into the shock wave passing down through the sample  $C$  and the rarefaction wave (if impedance of the material  $T$  is less than impedance of the standard material  $S$ ) reflecting up to the screen  $A$ . An ( $x$ - $t$ )-diagram in Fig. 2(a) shows the development of the shock wave process in the test assembly, where  $x$  is directed down and the coordinate origin is aligned with the position of

the rear surface of the flyer plate at the collision moment. After the shock wave, travelling with the velocity  $D_p$  through the sample, has approached the sample-gauge protector interface (at  $x = W_f + W_a + W_s$ ) and propagated through the protector plate  $E$ , the wave reflected from the free surface of  $E$  at the time moment  $t = t_5$ , accelerates the protector  $E$ , so the protector-pin gap is closed up at the time moment  $t = t_6$ , shorting the pin, which has initially been located at  $x = W_f + W_a + W_s + W_g + W_b$ .

The shock interaction process can also be tracked using the shock adiabat diagram drawn in the (P-U)-space (Fig. 2(b)). The shock adiabats are used in this coordinate system because a state after wave interaction is more conveniently described by a single point in the (P-U)-space. The right-going shock wave propagating into  $A$  gives a locus of states (a curve  $H_s$ ) connecting the initial state of the material  $S$  (state '[0]' at the origin corresponding to negligible pressure in the resting material) with all possible states behind the shock front; one of them is a state '[1]' at the impact surface when colliding the flyer plate with the screen. The left-going shock wave propagating into  $F$  sets up a curve that connects the initial state of the flyer plate '[0]' (it is under negligible pressure and its impact velocity is  $2U_0$ ) with all possible states behind the shock front; this curve  $H_s^-$  is the mirror image of  $H_s$ . Quite a strong assumption is made about the uniformity of the state '[0]', keeping in mind that the flyer plate is accelerated by an explosive charge within a small stand-off distance.

If the velocity of the flyer plate and properties of the standard material have been determined in the experiment, then the curves  $H_s$  and  $H_s^-$  can be drawn and a common pressure-velocity state  $(P_0, U_0)$  (state '[1]') behind the shock waves with the velocity magnitude  $D_s$  originating from the contact ( $A-C$ ) interface (at  $x = W_f$  in Fig. 2(a)) can be found as an intersection point of  $H_s$  and  $H_s^-$  (Fig. 2(b)). However, in the majority of the experiments the flyer plate velocity  $2U_0$  is not known a priori. Instead, the shock velocity  $D_s$  in the screen material is measured; more precisely, it is measured in the sample  $B$  attached to the screen at  $x = W_f$ , therefore, the assumption that the wave is stationary when propagating within the assembly  $A + B$  is essential. If  $D_s$  is known, then pressure and velocity behind the shock front in  $S$  are connected by the momentum equation of the system (1) resulting in a Rayleigh line  $P = \rho_s D_s U$  on the diagram in Fig. 2(b); here  $\rho_s$  is the initial density of the standard material. In this case the state '[1]' can be obtained as an intersection point of the shock adiabat  $H_s$  and the Rayleigh line as shown in Fig. 2(b). Pressure and velocity  $(P_0, U_0)$  calculated in such a way characterise the shock wave propagating through the screen  $A$  into the material  $T$  of the sample  $C$  under investigation (a part of the  $A + C$  assembly in Fig. 1).

After the moment  $t = t_1$  (Fig. 2(a)) when the shock wave enters the sample  $C$ , the shock wave breaks down on the  $A-C$  interface (at  $x = W_f + W_a$  in Fig. 2(a)) into the shock wave with velocity  $D_p$  going right into the sample  $C$  and the rarefaction wave going left back into the screen  $A$ . The reflection method (IM-method) assumes that the isentrope (curve  $R_s$  in Fig. 2(b)), linking states of the standard material with states behind the rarefaction wave, is very close to the reflected shock adiabat  $H_s^-$  (the mirror image of the incident shock adiabat  $H_s$ ). Similarly to the previous consideration for the standard material  $S$ , states for the material  $T$  under investigation behind the right-going shock wave propagating with velocity  $D_p$  lie on a Rayleigh line  $P = \rho_{00} D_p U$  in the (P-U)-space; here  $\rho_{00}$  is initial density of the material  $T$ . Thus, state '[2]' behind the shock front in the material  $T$  can be calculated as an intersection point of the Rayleigh line and the isentrope  $R_s$  (approximated by the curve  $H_s^-$  in the reflection

method). This state  $(P, U)$  in the pressure-velocity space gives a point of the shock adiabat  $H_p$  (Fig. 2(b)) for the material T. When P and U are found, the density behind the shock front is calculated from the mass conservation law (the first equation of the system (1)), which completes the process of calculating a point of the Hugoniot  $H_p$  sought. The shock velocity  $D_p$  could normally be calculated as  $W_s/(t_4 - t_1)$  that gives the average shock velocity, when ignoring possible shock wave attenuation (it starts at  $t = t_3$  in Fig. 2(a)). In real experiments, the pin shorting technique is used for the time of arrival registration. In the schematic of Fig. 2(a), the shorting of the pin occurs at  $t = t_6$  instead of at  $t = t_4$ , as described above. Similar time correction for the time of arrival of shock wave to the screen-sample interface should be made by taking account of the gauge set-up positioned at the screen-sample A-C interface at  $x = W_f + W_a$  (a schematic of the process for that gauge is not shown in Fig. 2(a)).

The most popular issue in the Hugoniot evaluation, which attracts the attention of many researchers (see, e.g., [31, 32]), is an approximation of the isentrope  $R_s$  by the reflected Hugoniot  $H_s^-$ . Less attention is paid to the non-steadiness of shock waves (kinetic behaviour of the waves) and conditions behind the shock front in porous materials. Recent advanced models consider the constitutive behaviour of porous material; for example, the P-lambda model by Grady [33] implemented in the CTH hydrocode and used for analysis of the shock wave structure in porous ceramic powders [34], a model by the author [24] used for analysis of shock profiles in porous aluminium [24] and dry and water-saturated sands [35]. Using advanced models, it is possible to describe the shock compression of a porous material with more details than with the traditional jump-like approximation of the shock front. In the present work we will ignore the issue of isentrope approximation, keeping in mind that the IM-reduced data for the porous copper reportedly were corrected for the approximated mirror adiabat to the isentrope. Thus, the present study will mainly concentrate on the issue of non-equilibrium behind the shock front. It should be mentioned that in the present work the rarefaction waves are computed directly via constitutive modelling. However, for analytical assessments (recovery of the shock velocity data from particle velocity), the mirror approximation will be used directly, because the source publications, reporting the IM-reduced data, do not reveal the nature and amount of the corrections.

### 3. Constitutive model

The constitutive model employed in the present work has been described elsewhere [24]. Briefly, for a porous material the model assumes two phases, each of which is characterised by density  $\rho$ , specific entropy  $s$ , pressure  $p$ , and temperature  $T$ ; the latter two being dependent thermodynamic variables. Velocity  $u$  is the same for both phases. For a porous material, the two phases are a gas (the air) and a solid phase with negligible strength. Variables for the corresponding phases 1 (gas) or 2 (solid) are referred to by superscripts in parentheses. Both phases are assumed to be compressible with individual mechanical properties. Using  $M$  for denotation of mass occupying specific volume  $V$ , the total mass and volume are  $M = M^{(1)} + M^{(2)}$  and  $V = V^{(1)} + V^{(2)}$ . Then the averaged density  $\rho = M/V$  relates to corresponding phase densities  $\rho^{(1)} = M^{(1)}/V^{(1)}$  and  $\rho^{(2)} = M^{(2)}/V^{(2)}$  via the volume and mass concentrations  $\theta$  and  $c$  of the first (gaseous) phase as follows

$$\theta = V^{(1)}/V, \quad c = M^{(1)}/M, \quad \rho = \theta \rho^{(1)} + (1 - \theta) \rho^{(2)} \quad .$$

Specific internal energy  $e$  and entropy  $s$  are

$$e = c e^{(1)} + (1 - c) e^{(2)} \quad , \quad s = c s^{(1)} + (1 - c) s^{(2)} \quad , \quad (2)$$

because of their extensivity. The entropy concentration for the first phase  $\chi$  is introduced in [24] similar to the introduction of the mass concentration. Following the definitions, we can express the independent phase state variables via the averaged ones:

$$\rho^{(1)} = \rho c / \theta, \quad \rho^{(2)} = \rho (1 - c) / (1 - \theta), \quad s^{(1)} = s \chi / c, \quad s^{(2)} = s (1 - \chi) / (1 - c) \quad . \quad (3)$$

Summarising, the independent variables that fully describe the two-phase material are  $\rho, s, u, c, \theta$ , and  $\chi$ . The first three variables are typical ones involved in the conservation laws:

$$\begin{aligned} \frac{\partial \rho}{\partial t} + \frac{\partial \rho u_j}{\partial x_j} &= 0, \\ \frac{\partial \rho u_i}{\partial t} + \frac{\partial (\rho u_i u_j + p \delta_{ij})}{\partial x_j} &= 0, \\ \frac{\partial \rho E}{\partial t} + \frac{\partial [\rho u_j E + p u_j]}{\partial x_j} &= 0, \end{aligned} \quad (4)$$

where  $E = e + u_j \cdot u_j / 2$  and  $\delta_{ij}$  are components of the unit tensor. When the specific internal energy  $e$  is given as a function of the parameters  $e = e(\rho, s, c, \theta, \chi)$ , the thermodynamic identity gives  $p = \rho^2 e_\rho$  and  $T = e_s$ .

We assume that the internal energy dependencies for each phase are given in the form

$$e^{(1)} = e^{(1)}(\rho^{(1)}, s^{(1)}) \quad , \quad e^{(2)} = e^{(2)}(\rho^{(2)}, s^{(2)}) \quad . \quad (5)$$

Thermodynamic identities for the phases can be used for calculation of averaged dependent variables from (2) as follows:

$$\begin{aligned} p &= \rho^2 e_\rho = \rho^2 (c e^{(1)} + (1 - c) e^{(2)})_\rho = \theta p^{(1)} + (1 - \theta) p^{(2)}, \\ T &= e_s = (c e^{(1)} + (1 - c) e^{(2)})_s = \chi T^{(1)} + (1 - \chi) T^{(2)}. \end{aligned} \quad (6)$$

Considering partial densities  $\rho^{(1)p} = M^{(1)}/V = \rho \cdot c$  and  $\rho^{(2)p} = M^{(2)}/V = \rho \cdot (1 - c)$ , we can associate the mass change of the first phase with the rate proportional to a constitutive function  $\varphi$ . Thus, the continuity equation for  $\rho^{(1)p}$  gives:

$$\frac{\partial \rho c}{\partial t} + \frac{\partial \rho c u_j}{\partial x_j} = -\rho \varphi. \quad (7)$$

Similarly, using the entropy balance equation, we can derive the following balance equation for parameter  $\chi$ :

$$\frac{\partial \rho \chi}{\partial t} + \frac{\partial \rho \chi u_j}{\partial x_j} = -\rho \omega, \quad (8)$$

where function  $\omega$  is a constitutive function responsible for the energy exchange between the phases. The constitutive equation for the volume concentration is considered in the following well-known form (see, for instance, references in [24]):

$$\frac{\partial \rho \theta}{\partial t} + \frac{\partial \rho \theta u_j}{\partial x_j} = -\rho \psi. \quad (9)$$

Thus, if for each phase the internal energy functions are taken in the form (5), the specific energy  $e(\rho, s, c, \theta, \chi)$  can be calculated from (2) with the use of (3). Pressure and temperature can be calculated from (6). The complete system of equations for the model contains equations (4), (7), (8), and (9). The system is fully defined when the equations of state for each phase (5) are pre-selected and the functions  $\varphi$ ,  $\psi$ , and  $\omega$  are given. The entropy increase condition from the energy balance equation imposes the following restrictions [24] for the functions  $\varphi$ ,  $\psi$ , and  $\omega$  that have to be chosen in the form

$$\varphi = e_c \cdot \varphi_0, \quad \psi = e_\theta \cdot \psi_0, \quad \omega = e_\chi \cdot \omega_0, \quad (10)$$

where functions  $\varphi_0$ ,  $\psi_0$ , and  $\omega_0$  are arbitrary non-negative functions. The expressions  $e_c$ ,  $e_\theta$ , and  $e_\chi$  can be calculated from (2, 5) and are associated with the affinities of the Gibbs potential, pressure and temperature [24].

Thus, the system (4) and the constitutive equations (7)-(9) generate a system describing the behaviour of two-phase porous material. The conservation laws are closed with the equations of state (5) for each phase, where parameters of the phases are connected with the averaged parameters by relations (2) and (3). The constitutive equations are closed with selection of the constitutive rates (the arbitrary non-negative functions  $\varphi_0$ ,  $\psi_0$ , and  $\omega_0$ ) that will be specified in next Section.

## 4. Constitutive relations for porous copper

We choose constitutive functions  $\varphi_0$ ,  $\psi_0$ , and  $\omega_0$  in the following form that has been used for the constitutive equations for sand and porous aluminium [24]:

$$\varphi_0 = c(1-c) \cdot A_0, \quad \psi_0 = \theta(1-\theta) \cdot B_0, \quad \omega_0 = \chi(1-\chi) \cdot C_0. \quad (11)$$

Here multipliers at the arbitrary non-negative functions were taken in the present form in order to keep conditions  $0 \leq c \leq 1$ ,  $0 \leq \theta \leq 1$ , and  $0 \leq \chi \leq 1$ , when solving numerically the constitutive equations of the model.

Similarly to [24] we specify  $B_0$  in the following form:

$$B_0 = a_{0A} \cdot [\theta - \theta_0(p)] , \quad (12)$$

where  $\theta_0(p)$  is determined as an inverted function of the equilibrium curve  $P_{\text{eqv}} = P_{\text{eqv}}(\theta)$  and  $B_0$  is equal to zero at  $\theta < \theta_0(p)$ . An example of derivation of the equilibrium curve has been shown in [24] for sand and porous 2024-Aluminium. Thus, the dependence  $\theta_0(p)$  is a stationary point of the solution of the constitutive equation (9) for the volume concentration parameter. The magnitude of the rate  $\psi$  is selected in such a way that the pore collapse time (the relaxation time for equation (9)) would be of the order of 10-100 ns as was assessed in [36]. To satisfy this assessment for the relaxation function  $\psi$  the constant  $a_{0A}$  is selected as  $a_{0A} = 2.5 \times 10^4 \text{ } \mu\text{sec}^{-1}$ .  $A_0$  and  $C_0$  are taken to be constant because data for the mass transformation and heat exchange are not available. As in the case of porous aluminium we select  $A_0 = 0$ . However, keeping in mind the extreme pressure range, we allow for a slow heat exchange with  $C_0 = 10^{-5} \text{ } \mu\text{sec}^{-1}$ ; in this case the rate  $\omega$  and corresponding rate for the heat exchange is of the order of 1 msec as assessed in [37].

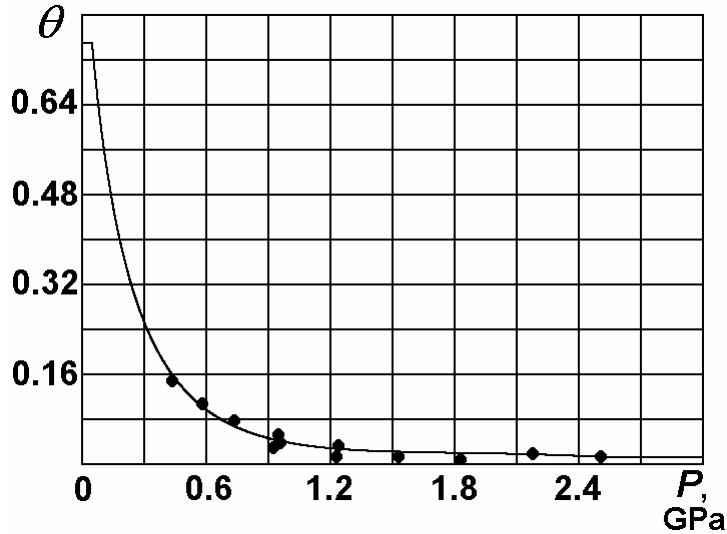


Fig. 3. Analytical fit of the equilibrium curve to the experimental points [15]

The data on the equilibrium curves can be obtained only from static compression data or assessed from the impact data recording complete stress profiles. Unfortunately, these data are not readily available for the copper powder with porosity  $m = 4$ . Therefore, we draw an analytical fit to the experimental data [15] for a porous copper with  $m = 1.4$ ; these experiments are shown in Fig. 3 by solid circles. The porosity  $m$  is related to the following volume concentration of the gaseous phase  $\theta = 1 - 1/m$  (in this formula only we neglect mass of gas when comparing it with mass of the solid phase within a volume). Therefore, the experimental points in [15] were found within the range of  $\theta$  from 0 up to  $1 - (1.4)^{-1}$  and an analytical formula for the equilibrium curve can be built up within this range. In order to use it for our case of the highly porous copper we extrapolate the analytical formula up to

$\theta = 1 - \frac{1}{4}p = 0.75$ . As a result, we pre-determine the analytical function to be constructed as follows:  $\theta_0(p) = 0.01215$  at  $p \geq 2.5$  GPa,  $\theta_0(p) = 0.75$  at  $p \leq 0.05$  GPa, and otherwise

$$\theta_0(p) = a_1 \cdot p^2 + a_2 \cdot p + a_3 + a_4 / p ,$$

where  $a_1 = -0.0269585$  GPa $^{-2}$ ,  $a_2 = 0.14122$  GPa $^{-1}$ ,  $a_3 = 0.763143$ , and  $a_4 = 0.161493$  GPa. The solid curve in Fig. 1 shows the constructed analytical function  $\theta_0(p)$  along with its comparison with the experimental data [15].

In order to close the model we must select EOSs for the two phases. The EOS for the gaseous phase was chosen in the following ideal gas form

$$e^{(1)}(\rho, s) = \frac{S_0}{\rho_{0a}(\gamma - 1)} \exp\left(\frac{s}{c_{va}}\right) \cdot \left(\frac{\rho}{\rho_{0a}}\right)^{\gamma-1} .$$

The EOS for the solid phase was taken in the following form [24], which is close to that of Mie-Gruneisen [38]:

$$e^{(2)}(\rho, s) = \frac{c_0^2}{2\alpha_0^2} \cdot \left[ \left( \frac{\rho}{\rho_{0s}} \right)^{\alpha_0} - 1 \right]^2 - \frac{p_0}{\rho} + c_{vs} T_0 \left( \frac{\rho}{\rho_{0s}} \right)^\beta \left[ \exp\left(\frac{s}{c_{vs}}\right) - 1 \right] + e_{j0} . \quad (13)$$

Material constants for the solid (copper) phase were taken to be  $c_0 = 3.94$  km/s,  $\rho_{0s} = 8.93$  g/cm $^3$ ,  $c_{vs} = 0.00045$  J/(g·grad),  $\alpha_0 = 0.96$ ,  $\beta = 2.03$ ,  $p_0 = 0.1$  MPa (1 bar),  $T_0 = 293$ °K. The standard values of constants were chosen for air at normal conditions with the exponent  $\gamma = 1.4$ , thermal capacity  $c_{va} = 0.001$  J/(g·grad), initial density  $\rho_{0a} = 0.0012$  g/cm $^3$ , and the constant  $S_0$  is calculated from the condition of normal pressure at the initial density of 0.1 MPa (1 atm);  $e_{j0}$  adjusts specific energies of the phases at the normal conditions.

The pressure response of an isotropic material to uniform omni-lateral dynamic compression (the  $(p, V)$ -curves) is always associated with a compression rate defined as follows

$$\dot{\varepsilon} = \frac{\partial u_1}{\partial x_1} + \frac{\partial u_2}{\partial x_2} + \frac{\partial u_3}{\partial x_3} . \quad (14)$$

For the quasi-static response the rate (14) is close to zero; in contrast, for the shock compression response it exceeds thousands of inverse seconds. In order to compare the  $(p, V)$ -curves with experimental pressure response data available in the literature, these curves have been calculated with the system of equations reduced to the case of uniform omni-lateral compression. Equations for this loading case are obtained from the general system of equations with the assumptions of a constant strain rate and uniform spatial deformation. As a result, the system (4), (7-9) is reduced to the following:

$$\begin{aligned} \frac{d \ln \rho}{dt} &= -\dot{\varepsilon}, \quad \frac{dc}{dt} = -\varphi, \quad \frac{d\theta}{dt} = -\psi, \\ \frac{d\chi}{dt} &= -\omega, \quad \frac{ds}{dt} = \frac{e_c \varphi + e_\theta \psi + e_\chi \omega}{T}. \end{aligned} \quad (15)$$

where  $d/dt = \partial/\partial t + u_j \cdot \partial/\partial x_j$ .

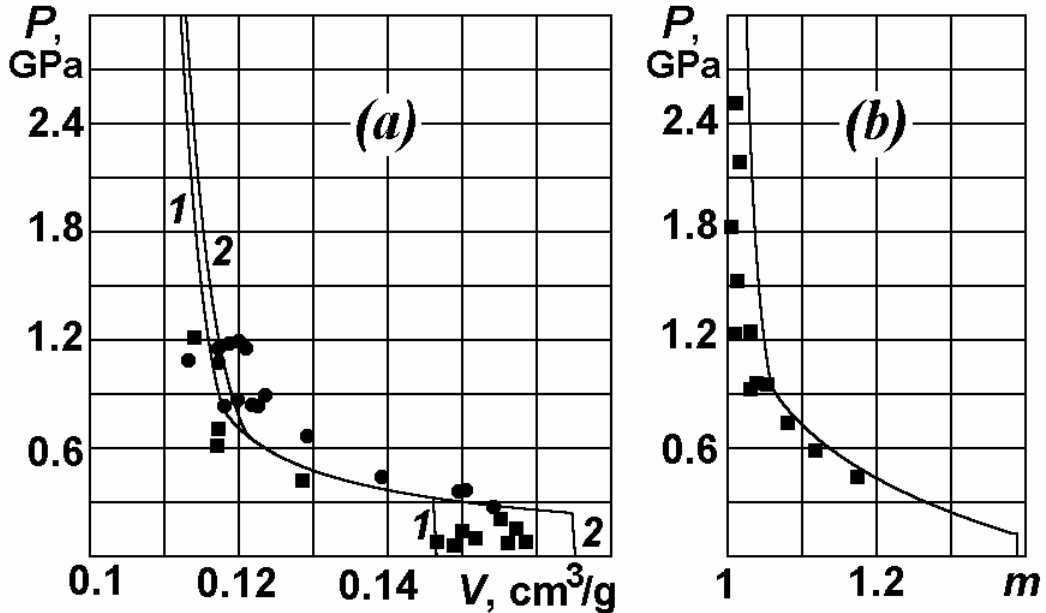


Fig. 4. The compression curves and comparison with the experimental data [14-16] (solid points)

Results of calculations using the system (15) at the strain rate of  $10^3 \text{ s}^{-1}$  are shown in Fig. 4, where specific volume is defined as  $V = 1/\rho$ . As it is seen from (15), solution of the system at a constant  $\dot{\varepsilon}$  describes the evolution of parameters with increments of specific volume following increments of time. Initial data for parameters  $c$  and  $\theta$  are determined from initial porosity,  $\chi$  is taken initially to be 0.5 in order to equally allow for the heat exchange between the phases, and  $s = 0$  (corresponds to normal initial temperature). The functions and constants  $A_0$ ,  $B_0$ , and  $C_0$  were selected as above with the parameter  $a_{0A}$  in (12) to equal  $2.5 \times 10^4 \mu\text{sec}^{-1}$ . Calculated  $(p, V)$ -curves in Fig. 4(a) correspond to initial densities  $\rho_{00} = 6.82 \text{ g/cm}^3$  (curve 1) and  $\rho_{00} = 6.052 \text{ g/cm}^3$  (curve 2) for porous copper. The curves are compared with experimental data (the solid points). The solid circles in Fig. 4(a) are data from [14] for a porous copper with initial density  $\rho_{00} = 6.052 \text{ g/cm}^3$ ; it should be noted that those data are related to pressure behind the shock front of the main wave versus 'final' density measured from the high velocity impact experiments [14-15], using a gas gun. The square points are data from [16] obtained in a similar way for a porous copper with initial densities between 6.31 and  $6.82 \text{ g/cm}^3$ . It should be noted that the loading conditions for these data can only be quite roughly approximated by a uniform omni-lateral load with a constant strain rate. Nevertheless, the compression curves are quite close to the experimental data seen in Fig. 4.

For relatively low velocities of impact, we believe that this is a reasonable fit for the case of a dynamic low strain rate compression.

The calculated curve in Fig. 4(b) shows pressure against current porosity for the porous (under-compacted) copper with initial porosity  $m = 1.38$  ( $\rho_{00} = 6.43 \text{ g/cm}^3$ ). Experimental points in Fig. 4(b) for a porous copper with initial density of  $6.43 \text{ g/cm}^3$  have also been obtained from gas gun experiments [15] and the same points were used in order to fit the curve shown in Fig. 3. This kinetic, which was obtained by fitting the constitutive equations within a range of porosities close to 1.4, will also be used for modelling the behaviour of shock compression of a highly compressed porous copper with porosity  $m = 4$ .

It should be noted that the curves in Fig. 4(a) quickly converge at higher pressures to the compression curve corresponding to the solid copper regardless of initial porosity and strain rate. It is interesting that the  $(p, V)$ -curves are non-convex, however, the equilibrium adiabatic condition  $\partial^2 p / \partial V^2 > 0$  at  $s = \text{const}$  takes place [24] and no singularities of the equation of state are required to describe this response. It should be noted that a phase transition could be described in the same way as well (see, for instance, a model considered in [39]).

## 5. Modelling of the shock behaviour of porous copper

The present numerical analysis is conducted within a one-dimensional set-up, using the Godunov method [40]. EOS and constitutive relations are used in the form specified in the previous Section. The Riemann problem (a necessary step of the Godunov method) for a porous material is solved by the method published in [41], which is briefly described in Appendix A.

First, we analyse the wave structure in a porous copper. For a pre-defined equilibrium curve the compaction time in the shock wave is affected by the time of pore collapse that is associated with deformation of the material matrix. In turn, the compaction time is affected by the parameter  $a_{0A}$ . Therefore, we calculate the wave propagation in porous copper with parameters and kinetics selected in the previous Section. The only variable will be the parameter  $a_{0A}$ . The initial density corresponds to the porosity of  $m = 4$  ( $\rho_{00} = 2.232 \text{ g/cm}^3$ ).

In order to observe how the pore collapse time, that is determined by the compression kinetic, affects the wave structure, we draw the wave profiles in Fig. 5 for the case corresponding to a relatively slow compaction ( $a_{0A} = 2.5 \times 10^1 \mu\text{sec}^{-1}$ ). Consecutive velocity and pressure profiles in a sample (the sample's thickness is 10 mm) of the material being compressed by a rigid plate moving with a constant velocity  $U_0$  correspond to the intervals shown in  $\mu\text{sec}$  against each profile throughout the present section.

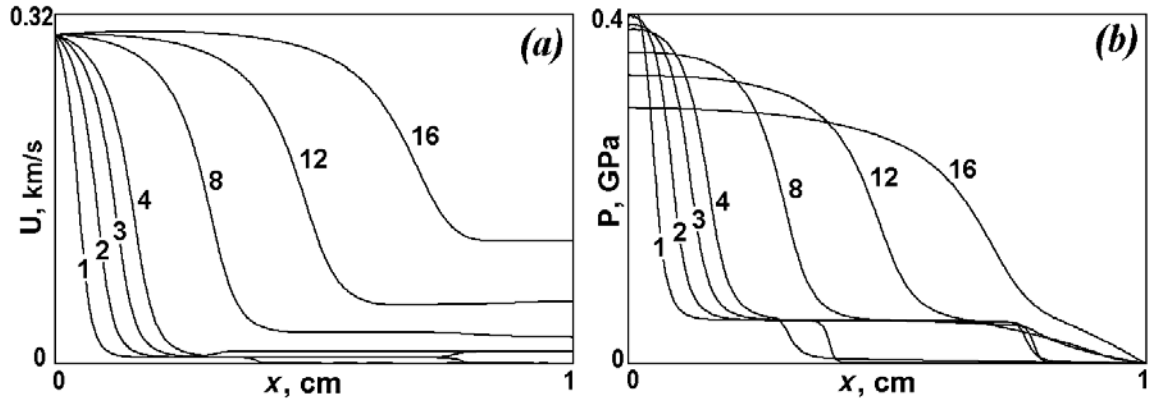


Fig. 5. The velocity (a) and stress (b) profiles at  $U_0 = 0.3 \text{ km/s}$  for the slow compression kinetics

Similar calculation has been conducted for a material with a quicker response to compression ( $a_{0A} = 2.5 \times 10^4 \mu\text{sec}^{-1}$ ), which corresponds to a more realistic pore collapse time as mentioned in the previous Section. Results are shown in Fig. 6 and demonstrate a significant distinction in the shock front width; however, the character of the loading, including evolution of the precursor and pressure attenuation of the main wave, has not changed significantly. It should be noted that variable  $x$  for the wave profile diagrams is the Eulerian coordinate stretched to the initial 1 cm space for every profile.

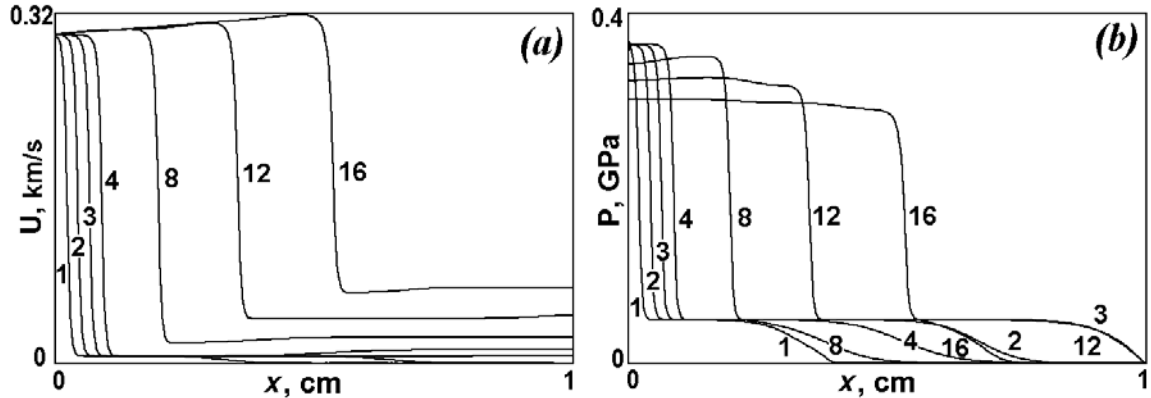


Fig. 6. The velocity (a) and stress (b) profiles at  $U_0 = 0.3 \text{ km/s}$  for the fast compression kinetics

It should be noted that the slow kinetic provides a pore collapse time interval of the order of 10  $\mu\text{sec}$ , whereas for the fast kinetic the collapse is a thousand times faster. This collapse time is related to the material structure; in particular, to the particle size and it is comparable with the closure time of a pore. For example, for a 50  $\mu\text{m}$ -porous material loaded by a shock wave with the pore walls moving with velocity of the order 1 km/s the closure time is 0.05  $\mu\text{sec}$ . This assessment is in agreement with the pore collapse times derived in [36, 37] as mentioned earlier. Therefore, the fast kinetic seems to be the more appropriate one.

In order to compare calculated shock profiles with experimental data we use information obtained in papers [14-16]. Unfortunately, the observed gauge traces are not available but the authors provided a schematic of the wave profiles with several control points of the profile contour. The gas gun experiments [14] were conducted with a plane sandwich set-up: a quartz 6.35 mm-flyer plate collided with porous copper ( $\rho_{00} = 6.43 \text{ g/cm}^3$ ) samples backed by another 6.35 mm quartz plate. The stress profiles were recorded at the two quartz sample interfaces. Results from the gauges (the control points of the wave profile contours for tests RA5 and RA2 from [14]) are shown in Fig. 7 by solid squares (test RA2 with the impact velocity of 0.1845 km/s and sample thickness 0.83 mm) and by solid circles (test RA5 with the impact velocity of 0.3073 km/s and sample thickness 1.03 mm). The points located at approximately 0.1  $\mu\text{sec}$  in Fig. 7 indicate the experimental pressure levels taken by the first gauge after equilibrium on the quartz sample surface (the impact surface). The remaining points relate to the wave recorded by the second gauge from the sample quartz interface of the target assembly.

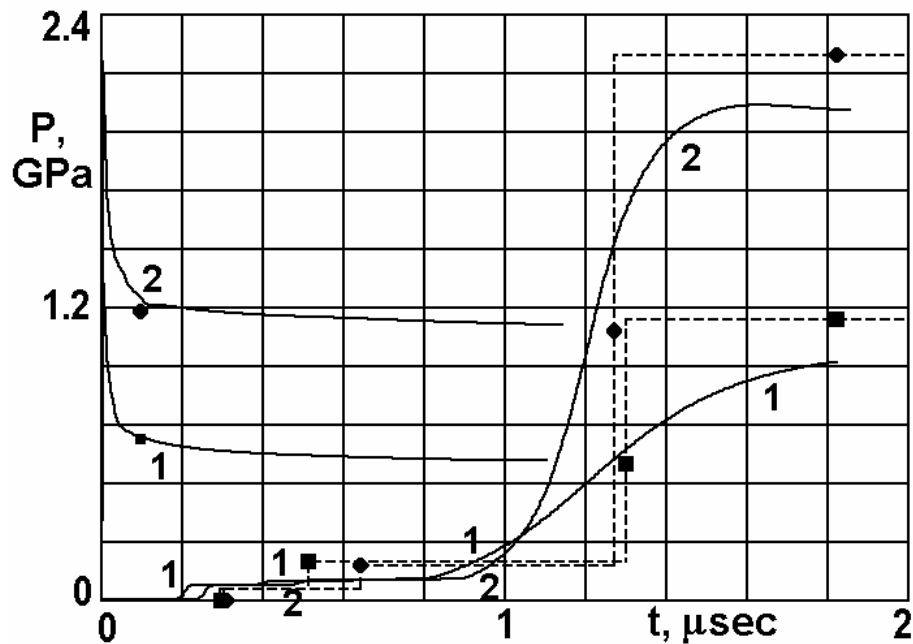


Fig. 7. The stress profiles of the test set-ups compared with the control points from the gas gun experiments [14]

In order to conduct calculations, the solid components of the assembly should be simulated as well. For the solid materials (components of the flyer plate, screen, backing plate, gauge, etc) the visco-elastic rate sensitive model [42] has been employed. The EOS [38] was used in the present work in the following form (which is close to (13)):

$$E(\rho, D, s) = \frac{c_0^2}{2\alpha_1^2} \cdot (\delta^{\alpha_1} - 1)^2 + 2b_0^2 \delta^{\beta_1} D + c_v T_0 \delta^{\gamma_1} \left[ \exp\left(\frac{s}{c_v}\right) - 1 \right]. \quad (16)$$

Here  $D$  is a second invariant of the elastic strain tensor [38] and  $\delta = \rho / \rho_0$ , where  $\rho_0$  is initial density. The strength effects are described by the model with use of the relaxation time function of shear stresses. A procedure of how this function can be obtained using two different yield limit points at two different strain rates has been described in [43]. Thus, the following material constants are required by the model for description of the behaviour of solid materials: density  $\rho_0$ , bulk modulus  $K = \rho_0 c_0^2$ , shear modulus  $G = \rho_0 b_0^2$ , the thermal capacity coefficient  $c_v$ , two compressibility coefficients (exponents in (16))  $\alpha_1$  and  $\beta_1$  for the modules  $K$  and  $G$ , and the Gruneisen coefficient  $\gamma_1$ . In the case of quartz components we selected constants in the relaxation function in such a way that the relaxation time would be large enough during the deformation process; then, the quartz responds nearly elastically when interacting with the porous samples.

For quartz we selected the following constants for the EOS (16);  $\rho_0 = 2.203 \text{ g/cm}^3$ ,  $K = 37 \text{ GPa}$ ,  $G = 32 \text{ GPa}$ ,  $c_v = 0.01 \text{ J/(g·grad)}$ ,  $\alpha_1 = 1.07$ ,  $\beta_1 = 3$ , and  $\gamma_1 = 1.117$ . We used the fast compaction kinetic ( $a_{0A} = 2.5 \times 10^4 \text{ } \mu\text{sec}^{-1}$ ) in all calculations below. The wave structure tracked by the second gauge at the rear side of the sample gives the start of the precursor (solid points nearly  $0.3 \text{ } \mu\text{sec}$  in Fig. 7), pressure level of the second step behind the precursor (time of arrival and pressure level identified by the solid points at the breaks of dashed lines), the middle-point of the main compression wave (solid points at nearly  $1.3 \text{ } \mu\text{sec}$  in Fig. 7), and amplitude of the main wave (indicated by solid points at  $t = 1.8 \text{ } \mu\text{sec}$ ). Thus, the experimental profiles are characterised schematically by the dashed lines passing through the solid circles for the test RA2 and through the solid squares for the test RA5.

Corresponding calculations are drawn by line 1 for the test RA2 and by line 2 for the test RA5. It is remarkable that the second pressure increase after the precursor is observed in the calculation as well; it appears from the calculations that this second rise is actually associated with the pressure build up due to interaction of the reflected precursor from the sample-quartz interface with the main compression wave and transmission of the second double-load precursor to the interface after the interaction. It is interesting that similar precursor reverberation has been observed in reverberation tests [16]. Distinct precursors have been observed experimentally in other porous materials as well (e.g., for aluminium powder, typical wave profiles have been reported in [23]). Thus, we believe that the constants selected for porous copper are satisfactory for description of these features of the powder shock compression and all subsequent analysis will be conducted with the present constants.

Further analysing profiles obtained in Fig. 6, we can draw the density and volume concentration profiles as shown in Fig. 8. It is seen that for the case of a relatively low impact load the wave non-equilibrium is chiefly governed by interaction of the precursor wave reflected from the free surface with the main compression wave. When evolving, the particle velocity behind the front gradually rises (after interaction with the precursor), pressure drops, and density remains unchanged.

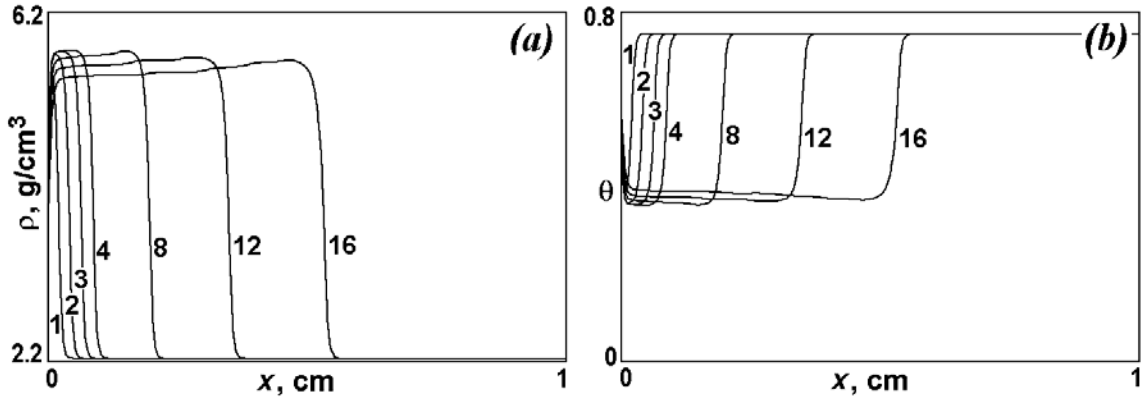


Fig. 8. The density (a) and volume concentration (b) profiles for the wave at  $U_0 = 0.3 \text{ km/s}$

When increasing the load strength the wave structure changes. The following two figures show profiles for the waves when loaded with a driver velocity of  $U_0 = 1 \text{ km/s}$ . Consecutive wave profiles in Figs. 9-10 correspond to 1.5, 3, 4.5, and 6  $\mu\text{sec}$ .

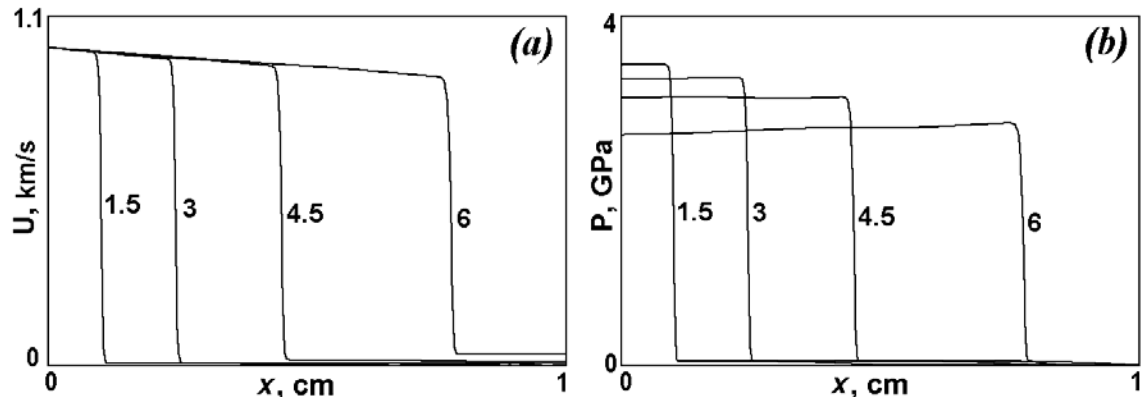


Fig. 9. The velocity (a) and stress (b) profiles for the wave at  $U_0 = 1 \text{ km/s}$

The influence of the precursor in this case is still noticeable but not so strong because the precursor velocity is only double the velocity of the main compression wave. In this case evolution of the wave profile is almost entirely governed by the compaction process and this only slightly alters the pressure profile from uniformity. Corresponding density and volume concentration profiles are drawn in Fig. 10. It is seen from Fig. 9 that the particle velocity is not significantly changing within any particle in this nearly Lagrangian coordinate system (the apparent non-uniformity in the space between the wave profiles should be commented as this is associated with the coordinate transformation; in fact, after reduction of the profiles to the real Eulerian position, the distance between profiles is practically constant with time). However, pressure gradually drops, allowing for rearrangement of the solid matrix and equilibrating pressure within the matrix and air. At the same time, density is gradually increasing along with the volume concentration of the solid phase due to expansion of the

initially compressed solid phase into the gaseous phase. From the viewpoint of state evolution behind the shock front, the velocity and pressure drop, whereas density remains unchanged.

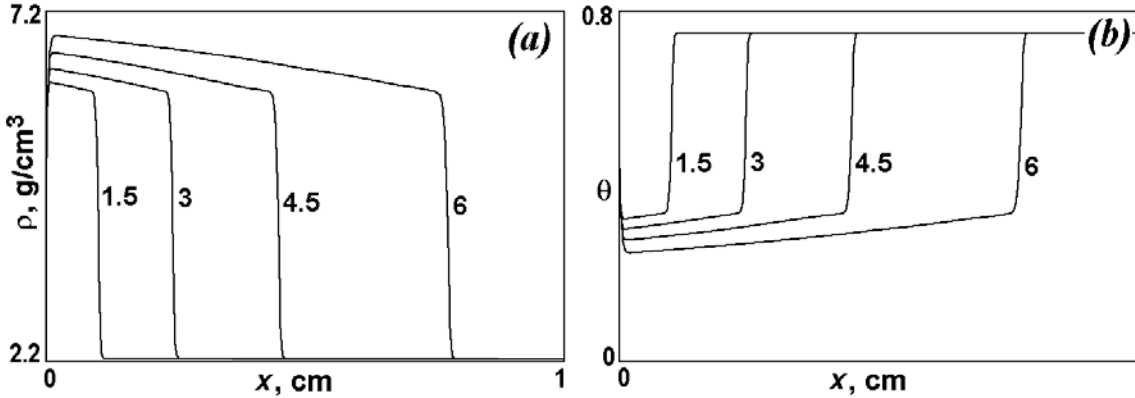


Fig. 10. The density (a) and volume concentration (b) profiles for the wave at  $U_0 = 1 \text{ km/s}$

Pressure is equilibrating relatively quickly via relaxation of the parameter  $\theta$  where a stationary point is achieved at  $e_\theta = 0$  (i.e., when the phase pressures equilibrate). Within this range of loads the material state behind the front undergoes a slow heat exchange, equilibrating the temperature via relaxation of the parameter  $\chi$  with a stationary point achieved at  $e_\chi = 0$  (i.e., when the phase temperatures equilibrate). The parameter evolution directly behind the main shock front might be explained by the two-stage character of the load headed by the precursor. Comparing two elements of the material, the first of which is close to the loading surface and the second is in the middle of the sample we can analyse the process of deformation. Both elements are compressed to approximately the same volume. However, the first is loaded by a (practically) one-step load; therefore, the pressure and temperature are higher than for the second element, for which the loading is closer to isentropic (farther from the shock-like). The second element is subjected to a two-step loading because the relaxation is taking a longer time. These processes are manifested in the whole response of material shown in the calculations of Figs. 9 and 10. It should be noted that the deformation physics is associated very closely with the mechanisms of compression and heat exchange governed by the kinetic chosen. Another example of the wave behaviour will be given in the Discussion Section.

To complete the analysis, propagation of a fairly strong shock wave has also been calculated with a driving plate velocity of  $U_0 = 3 \text{ km/s}$ . Consecutive profiles in Figs. 11-12 correspond to the time moments of 0.5, 1, 1.5, and 2  $\mu\text{sec}$ . It is seen from Fig. 11 that in this case the precursor effect is almost negligible. Corresponding profiles for density and volume concentration of the gaseous phase are drawn in Fig. 12. It is also seen from these figures that in this case the shock wave is almost fully stationary with a relatively small drift of velocity and pressure directly behind the shock front due to the heat exchange effects. It should be noted though that the trend remains the same as in the preceding calculation. If the load is further increased, the deformation is closer to a one-step loading because the main wave overtakes the precursor.

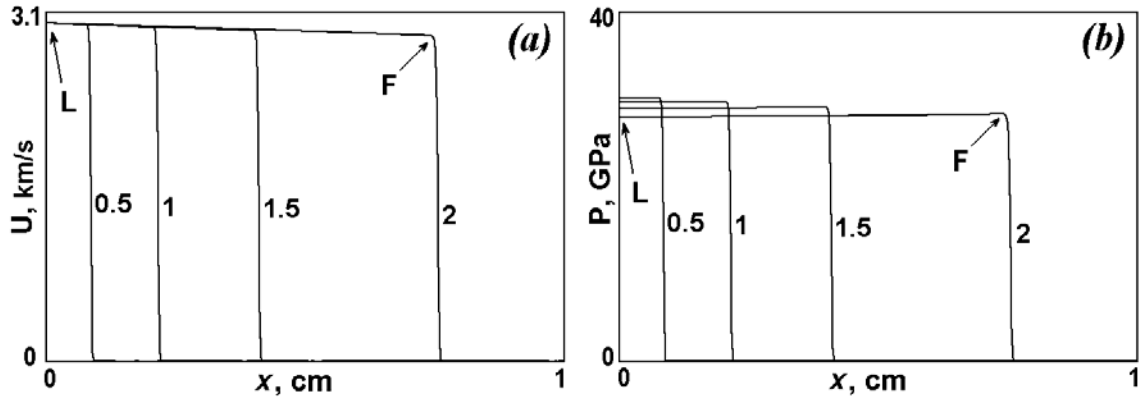


Fig. 11. The velocity (a) and stress (b) profiles for the wave at  $U_0 = 3 \text{ km/s}$

Thus, the constitutive modelling of shock propagation in porous copper shows a disagreement between the parameters ( $U_L, P_L, \rho_L$ ) at the loading surface (piston) and the parameters ( $U_F, P_F, \rho_F$ ) directly behind the shock front. The characteristic points of the profile 4 in Figs. 11-12 are marked by arrows and labelled by letters 'L' and 'F', correspondingly.

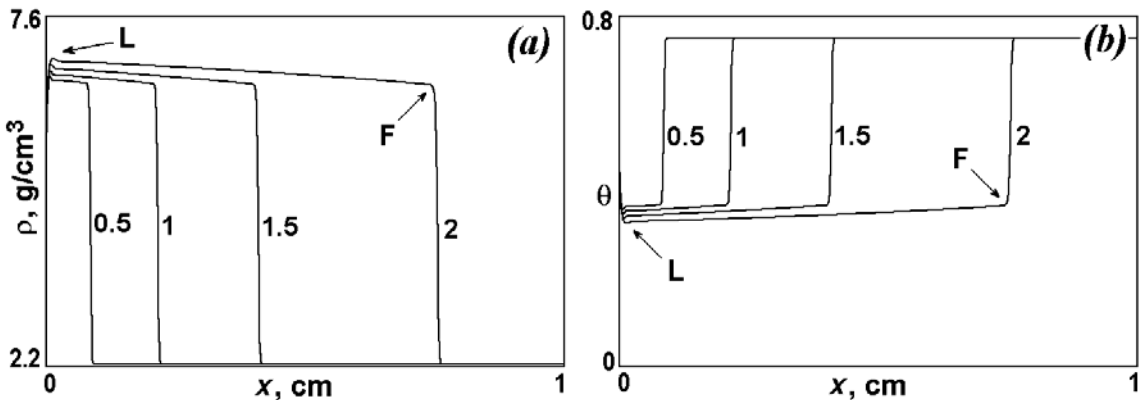


Fig. 12. The density (a) and volume concentration (b) profiles for the wave at  $U_0 = 3 \text{ km/s}$

It is interesting to note that the percentage deviation  $(U_L - U_F)/U_L$  increases from approximately -7% first (it is negative in this case because of the precursor effect) to 5-7% as seen from comparison of the results in Figs. 6-9(a); after that it decreases down to approximately 2-3% when comparing the results from Fig. 9(a) and Fig. 11(a). This situation contrasts with that for a solid material where the jump-like approximation of the shock wave due to a constant load is very good for the load range where the strength and phase transition effects can be ignored. This is an alarming fact because traditionally, when using the jump-like approximation, the Hugoniot density is calculated from the following relation from system (1):  $\rho = \rho_0 \cdot D / (D - U)$ , where  $U$  is presumed to be a constant velocity (the loading velocity) behind the shock wave. Because this is not so in the present case, we evaluate Hugoniots in the next Section from direct calculations of states behind the shock wave, using the set-ups and input data recovered as closely as possible to the ones published in the literature.

## 6. Brief description of available experiments

Focusing on the tests for porous copper with porosity  $m = 4$ , we list all available experimental data in Table 1. We limit our consideration to data for the pressure range lower than 200 GPa. The Table lists 17 data points from publications [6-9, 11-12]. The Table includes the IM-reduced data of the particle velocity  $U$  and the shock velocity  $D$  (in km/s) for copper powders. As was mentioned earlier, the data from [6-9] were reportedly subject to another reduction that included a data correction via elimination of the wave attenuation effect. As was described in Section 2, the particle velocity  $U$  was calculated for the reduced data, using the Impedance Mismatch (IM) method. The procedure of calculation of the particle velocity with the IM-method is described in Appendix B; formula (24) in the Appendix gives the method of calculation for the particle velocity  $U_h = f(D, U_0)$  that is denoted by  $U$  in the present Section. While using an inverse procedure, we can recover the data  $U_0$  in the screen (from the values of  $U_h$  and  $D$  that are listed in the experimental works), using tabulated Hugoniots for the screen materials, where the Hugoniots are usually presented as linear particle velocity-shock velocity dependencies

$$D = a + b \cdot U \quad . \quad (17)$$

The screen material that was used for the tests in [6, 7] is the Russian analogue (AD-1) of the aluminium 1100-O alloy as reported in [44]. The Hugoniot that was used for the IM-reduction was reported in [7] as follows:

$$D = 5.333 + 1.356 \cdot U \quad . \quad (18)$$

Thus, using the Hugoniot for drawing the shock adiabat in the  $(P, U)$ -space with the help of the diagram in Fig. 2(b), we can recover state '[2]' that is characterised by the parameters  $(P_0, U_0)$ . We will denote the particle velocity behind the shock front by  $U_{scr}$  in the present Section. Then, using  $U_{scr}$ , we can calculate  $D_{scr}$  from (17).

After doing this with the assumption that the screen for all the tests is made from the aluminium alloy, all recovered screen data have been listed in Table 1. Reported screen data (the particle velocity) is available for point 5 only, and the data restored from the  $(U, D)$ -data for this point reproduce the experimental  $U_{scr}$  value quite well. Screen materials are not known for points 7, 11, 13, and 17 and, therefore, we assumed the aluminium alloy for the screen by default. Initial densities for porous powders of points 7 and 11 slightly deviate from the porosity  $m = 4$ ; when restoring the screen data and conducting constitutive modelling we always used the actual density values for the corresponding experiments (these values are shown in the references/comments column followed by ' $\rho$ '). Points 14 and 15 were actually obtained with iron screens and the particle velocities that were measured in the experiments along with the shock velocities in the screens are shown in the references/comments column followed by 'Fe'. The listed screen data  $U_{scr}$  and  $D_{scr}$  for these points is a result of recalculation for the aluminium screen, using the  $(U, D)$ -pairs reported in [8, 9].

Table 1. The Hugoniot velocity data from available experiments

N	Uscr	U	D	Dscr	P	$\rho$	Ref., Comments
1	0.37765	0.661	0.946	5.845	1.395	7.402	[6]
2	0.765	1.235	1.66	6.37	4.572	8.71	[6]
3	1.135	1.725	2.33	6.87	8.963	8.588	[6]
4	1.46	2.12	2.93	7.31	13.852	8.066	[6]
5	1.95	2.68	3.84	7.97	22.95	7.382	[7]
6	2.12	2.89	4.07	8.209	26.23	7.6916	[6]
7	2.514	3.33	4.662	8.74	35.132	7.921	[11], $\rho(2.263)$
8	2.69	3.51	5.10	8.98	39.92	7.153	[6]
9	2.918	3.77	5.41	9.29	45.483	7.356	[6]
10	3.288	4.16	6.07	9.79	56.31	7.087	[6]
11	3.472	4.4	6.248	10.04	60.536	7.445	[11], $\rho(2.202)$
12	3.716	4.61	6.81	10.37	70.01	6.903	[6]
13	4.94	6.00	8.325	12.033	111.4	8.0	[12]
14	5.147	6.15	8.96	12.31	122.88	7.1106	[8], Fe(4.15,11.05)
15	5.315	6.42	8.79	12.54	125.8	8.27	[9], Fe(4.26,10.67)
16	5.615	6.68	9.51	12.946	141.665	7.4937	[6]
17	6.8	8.0	11.028	14.56	196.7	8.146	[12]

Using the velocities U and D (in km/s), pressure (in GPa) and density (in g/cm<sup>3</sup>) are calculated with the relations (1) and are also shown in Table 1 in the P- and  $\rho$ -columns. Points 1 and 2 were possibly measured by piezoceramic sensors, according to [6], and the others by the pin technique. According to [6], one of the points was possibly found for a sample with evacuated air. This sample had to be cased in order to allow for the evacuation. However, no information about the test conditions, including set-up, initial parameters, and quality (homogeneity) of the material after the air evacuation, was reported, therefore, this point cannot be adequately modelled.

It is seen from the (P,  $\rho$ )-data in Table 1 that the apparent abnormality is clearly exhibited by elevated densities for points 2, 3, and 4; all these points were reported in [6]. At the same time, as we observed in the previous Section, the velocity range covering these points is within the range where the velocity non-equilibrium behind the shock front is most noticeable. This fact will be paid special attention in the next modelling Section.

The experimental design for tests [6] was described in greater detail in recent publications [1, 25]. These papers show a general set-up for the plate impact experiment, which is close to the schematic in Fig. 1; in reality, the set-up is complemented with a Plane Wave Generator (PWG) spaced by an air gap to the flyer plate. The PWG and air gap dimensions were not reported. The screen material for the majority of experiments was reported to be the aluminium 1100-O alloy; two points 14 and 15 were reported in [8, 9] to be obtained with steel screens. Because the abnormality was observed for tests with the aluminium screens, we pay special attention to the set-up with the aluminium screen. According to [6, 25-27], the sample thickness varied from 1.5 to 5 mm and for the flyer and screen plates varied from 2 to 5 mm. Keeping in mind that the shock attenuation effects are minimal for the thickest flyer and screen plates and the thickness distribution over the experiments' set is not reported, we

selected a set-up with favourable geometrical parameters in order to minimise the wave attenuation, i.e., thickness of the plates was selected to be 5 mm. It is expected that thickest sample correspond closer to stationary conditions, therefore, for the basic set-up we selected the sample thickness to be 5 mm as well.

In order to analyse possible effects of the set-up geometry variation we set the screen thickness to be 5 mm and selected two options for the flyer plate thickness. The first, where the wave attenuation effects are possible, is with a flyer plate thickness of 5 mm. The second is with thicker flyer plates (from 6 to 15 mm, depending on the impact velocity), which eliminates the wave attenuation factor.

## 7. Results of modelling the shock compression tests

This Section simulates the conditions of the shock compression tests described in the previous Section as closely as possible. Because the specifications of the explosive charges accelerating the flyer plates were not known, we assumed that each flyer plate had a constant velocity  $2U_{scr}$  with  $U_{scr}$  specified in respective column of Table 1. Two cases were considered for the study of possible influences of the wave attenuation on the calculation results. Conditions of the first case presume that thickness of the flyer plate is variable such that the time  $t_3$ , when the shock wave in the porous sample is overtaken by the rarefaction wave from the free surface of the flyer plate, would be not less than the time of registration of a signal at  $t = t_6$  (see Fig. 2(a)). For example, with the basic set-up for low impact velocities (points 1-5 in Table 1) the flyer plate thickness should be not less than 15 mm and for high impact velocities (points 13-15) – not less than 6 mm. The second case reproduces the best-reported experimental set-up (from the viewpoint of minimal wave attenuation) with a fixed flyer plate thickness of  $W_f = 5$  mm (Fig. 2(a)). The screen's thickness was fixed to  $W_a = 5$  mm. For the basic set-up the sample's thickness was selected to be 5 mm as well ( $W_s = 5$  mm in Fig. 2(a)).

Determination of the shock wave arrival numerically is subjective because it is associated with a preferred choice of the characteristic point on the shock profile in order to calculate the profile's velocity. To eliminate this factor, we attempted to reproduce the experimental set-up down to the level of the gauge assembly. To realise this in the calculation, we attached to the rear surface of a sample (at  $x = W_f + W_a + W_s$  in Fig. 2(a)) a thin aluminium plate of thickness  $W_b = 0.2$  mm (see Fig. 2(a)), which could be associated with the end wall of the protective cup  $E$  of the gauge  $G$  in Fig. 1. In the calculation runs we traced the free rear surface of the plate until it reached the point  $x = W_f + W_a + W_s + W_b + W_g$  at  $t = t_6$ , where the gap space  $W_g$  was selected to be 0.2 mm as well. This time is considered to be the time of arrival of the shock wave to the free surface of the sample (at  $x = W_f + W_a + W_s$  in Fig. 2(a)).

Normally two runs were calculated where the first one was with the sample removed from the numerical set-up. For this run the time of arrival  $t_1$  of the wave at the point  $x = W_f + W_a$  was incremented by the time of propagation of the shock wave through the gauge cup and the time of closing the gap  $W_g$  (for the set-up with the sample shown in Fig. 2(a) this increment corresponds to  $t_6 - t_4$ ), resulting in the time moment  $t_1'$ . Thus, the averaged shock wave velocity  $D_{cal}$  in a porous sample was calculated as  $W_s / (t_6 - t_1')$ . The material states for

calculation of Hugoniots were taken at the time moment when the shock wave starts moving the sample-cup interface (an element of the material at  $x = W_f + W_a + W_s$ ). Similarly, the shock velocity in the screen was calculated in the same set-up by simply replacing the investigated material T in the area  $W_f + W_a < x < W_f + W_a + W_s$  by the standard material S. It should be noted that in our calculations we tested aluminium, copper, or steel as the cup's material, and we did not notice an essential difference in calculated shock velocity, as the cup's specific mass did not change dramatically.

For the aluminium 1100-O alloy standard material, we selected the following constants for the EOS (16);  $\rho_0 = 2.712 \text{ g/cm}^3$ ,  $K = 68.8 \text{ GPa}$ ,  $G = 27 \text{ GPa}$ ,  $c_v = 0.0009 \text{ J/(g·grad)}$ ,  $\alpha_1 = 1.0$ ,  $\beta_1 = 3.577$ , and  $\gamma_1 = 1.088$ . Two points used for the shear stress relaxation kinetics fitted with the use of the method [44] were taken from [45] as the yield limit  $Y$  against strain rate:  $Y_1 = 0.0965 \text{ GPa}$  at  $\dot{\epsilon}_1 = 1.8 \text{ sec}^{-1}$  and  $Y_2 = 0.124 \text{ GPa}$  at  $\dot{\epsilon}_2 = 2600 \text{ sec}^{-1}$ . The constitutive equations for the porous copper were used with the fast compaction kinetics, specifying  $a_{0A} = 2.5 \times 10^4 \text{ μsec}^{-1}$ .

Table 2. Calculation results for the basic set-up and comparison with the experiments

N	Dcal	Dexp	Ucal	U'c	Uexp	Dscal	Dsr	$\rho_{\text{cal}}$	$\rho_{\text{red}}$
1	0.995	0.946	0.64	0.66	0.661	5.78	5.845	5.86	7.402
2	1.837	1.66	1.173	1.21	1.235	6.27	6.37	6.06	8.71
3	2.55	2.33	1.64	1.69	1.725	6.79	6.87	6.19	8.588
4	3.14	2.93	2.04	2.09	2.12	7.25	7.31	6.29	8.066
5	3.96	3.84	2.6	2.66	2.68	7.95	7.97	6.46	7.382
6	4.24	4.07	2.79	2.86	2.89	8.19	8.209	6.51	7.6916
7	4.88	4.662	3.33	3.3	3.33	8.76	8.74	6.68	7.921
8	5.14	5.10	3.43	3.5	3.51	9.01	8.98	6.69	7.153
9	5.49	5.41	3.7	3.75	3.77	9.34	9.29	6.76	7.356
10	6.06	6.07	4.09	4.16	4.16	9.87	9.79	6.87	7.087
11	6.35	6.248	4.3	4.39	4.4	10.13	10.04	6.871	7.445
12	6.7	6.81	4.55	4.63	4.61	10.48	10.37	6.99	6.903
13	8.48	8.325	5.9	5.97	6.00	12.23	12.033	7.32	8.0
14	8.8	8.96	6.1	6.18	6.15	12.52	12.31	7.37	7.1106
15	9.04	8.79	6.29	6.37	6.42	12.76	12.54	7.41	8.27
16	9.44	9.51	6.6	6.69	6.68	13.19	12.946	7.48	7.4937
17	11.1	11.028	7.9	7.97	8.0	15.06	14.56	7.74	8.146

The state behind the shock front was assessed in the same manner as the state  $F$  (will also be referred to as F-state below) in Figs. 11-12. Calculation results for the first case (when setting up thick flyer plates in order to eliminate the wave attenuation effect) are listed in Table 2 along with experimental shock velocities, IM-reduced particle velocity and density ( $\rho_{\text{red}}$ ) transferred from Table 1. In the Table,  $D_{\text{cal}}$  and  $D_{\text{exp}}$  are the calculated and experimental shock velocities in porous sample,  $U_{\text{cal}}$  and  $U_{\text{exp}}$  are the calculated (F-velocity) and experimental (IM-reduced) particle velocities in the sample,  $D_{\text{scal}}$  and  $D_{\text{sr}}$  are the calculated and experimental (IM-recovered from  $D_{\text{exp}}$  and  $U_{\text{exp}}$ ) shock velocities in the screen, and  $\rho_{\text{cal}}$  is the calculated density (F-density) in the sample. It is seen that the velocities are in a good agreement. Moreover, in order to eliminate the screen effect because of a possible mismatch of a material

described with the use of the present EOS, with the actual aluminium material used in the tests, we can repeat the procedure of elimination of the screen data by recalculation of the particle velocity  $U'_c$  in the material investigated, using the equation (24) in Appendix B.

Then, using calculated shock velocity  $D_{cal}$  we can draw the Rayleigh line (shown in Fig. 2(b) with the shock velocity denoted by  $D_c$ ) and compare the velocity  $U'_c$  (denoted by  $U'$  in Fig. 2(b)) with the experimental values (these values were obtained in [6-12] by the IM-reduction procedure from un-reported experimental shock wave velocities in the screen and in the porous sample followed by a post-correction for the wave attenuation effects). It is seen that after applying this screen elimination correction, the agreement of  $U'_c$  and  $U_{exp}$  is remarkable (the largest disagreement for the whole dataset is approximately 2%). However, the densities are in a significant disagreement (for the first 6 points the minimum disagreement is 12.5% and the largest is over 30%). Therefore, the procedure of density determination is likely to be an issue; as error estimates in Appendix B show, the density error increases with the porosity proportionally. Similar error estimates for density are quite common and reported in various sources (e.g., see [1, 21, 46]).

The velocity data from Table 2 are summarised in Fig. 13, where crosses correspond to the experimental points  $D_{exp}$  (shown in the figures below as  $D_p$  for the tested material and  $D_s$  for the screen material) and  $U_{exp}$ ; the solid circles correspond to the present calculation results  $D_{cal}$  and  $U_{cal}$  for the tested material and  $D_{scal}$  and  $U$  (not listed in Table 2) for the screen material.

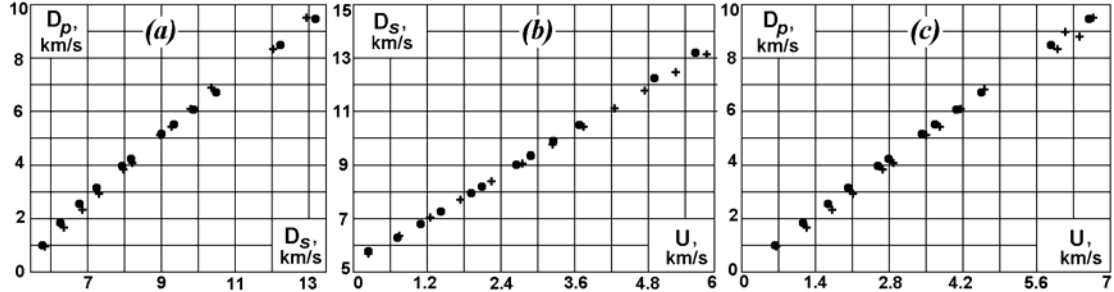


Fig. 13. The  $(D-D)$ -dependence for the basic set-up (a) and the  $(D-U)$ -dependencies for the standard (b) and for the investigated material (c) with elimination of the shock attenuation effects. The calculations (solid points) are compared with the experiment (crosses)

For the case, when thickness of the flyer plate is fixed to 5 mm, the wave attenuation effects are more significant at low impact velocities because the shock velocity  $D_s$  in the porous material is substantially lower than the sound velocity in the standard, resulting in the time of start of the wave attenuation ( $t_3$  in Fig. 2(a)) to be less than the time of arrival of the shock wave to the free surface ( $t=t_4$ ). Corresponding calculated data are shown in Fig. 14. It is seen from Fig. 14 that the velocity results are quite similar to the previous case, however, the influence of the wave attenuation on the  $(D-U)$ -dependence for the tested material in the region of maximum influence of the wave attenuation factor (the low impact velocity region) is more distinct.

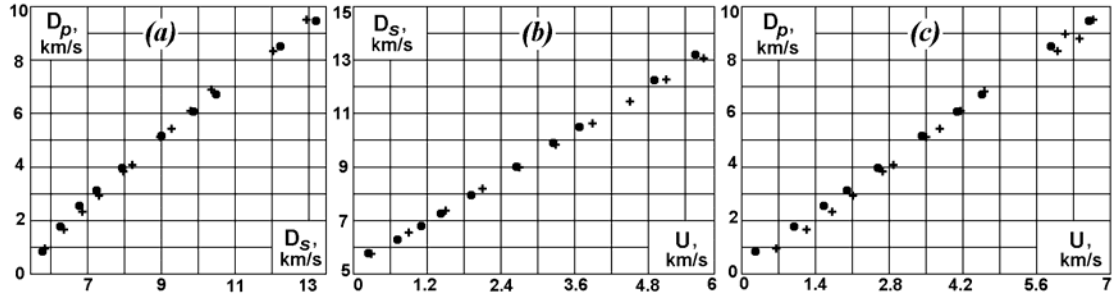


Fig. 14 The (D-D)-dependence for the basic set-up (a) and the (D-U)-dependencies for the standard (b) and for the investigated material (c) with the shock attenuation effects in place. The calculations (solid points) are compared with the experiment (crosses)

It should be mentioned that the disagreement between the calculated and experimental shock velocity might appear quite significant (up to 9% in a worst scenario). However, when running calculations with the wave attenuation effects there is a deviation in the velocity values; this deviation exhibits an essential contribution of the wave attenuation correction procedure, unfortunately, this procedure was not documented for the present experiments. For example, the calculated shock velocities for the first and second points (with wave attenuation) transform to  $D_{cal} = 0.843$  km/s and  $D_{cal} = 1.77$  km/s; this gives a variability for the first point from +5% to -10% and a variation from +9% to +6% for the second point, and so on. Such variations quickly decrease when moving from the non-equilibrium low pressure area into the area where the jump-like approximation is more appropriate; for example, for the data in Table 2, the disagreement decreases to 1-2% for data points 7 and above.

In order to more clearly demonstrate the difference between the two cases after data IM-reduction, we draw the Hugoniots ((P,V)-response curves). These curves are shown in Fig. 15. The first set of points (circles through which a curve 1 is drawn) corresponds to calculated pressure and density behind the shock front (the F-pressure and F-density). The second set of points (squares through which a curve 2 is drawn) correspond to pressure and density calculated according to the mass and momentum balance across the shock wave expressed by the system of equations (1); the shock velocity and particle velocity values were taken from the present calculations as  $D_{cal}$  for the shock velocity and  $U'_c$  for the particle velocity. Crosses in Fig. 15 show the experimental (P-V)-points (IM-reduced data) listed in the literature. Fig. 15(a) shows the Hugoniots for the case, where the shock attenuation effects are eliminated; Fig. 15(b) shows similar curves for the basic set-up with shock attenuation affecting the data.

The calculated Hugoniots show quite a significant deviation of the states achieved directly behind the shock front (curves 1) from the states calculated with the help of equation (24) using given  $U_0$  and  $D_{cal}$  (curves 2 were obtained with the IM-procedure of data reduction).

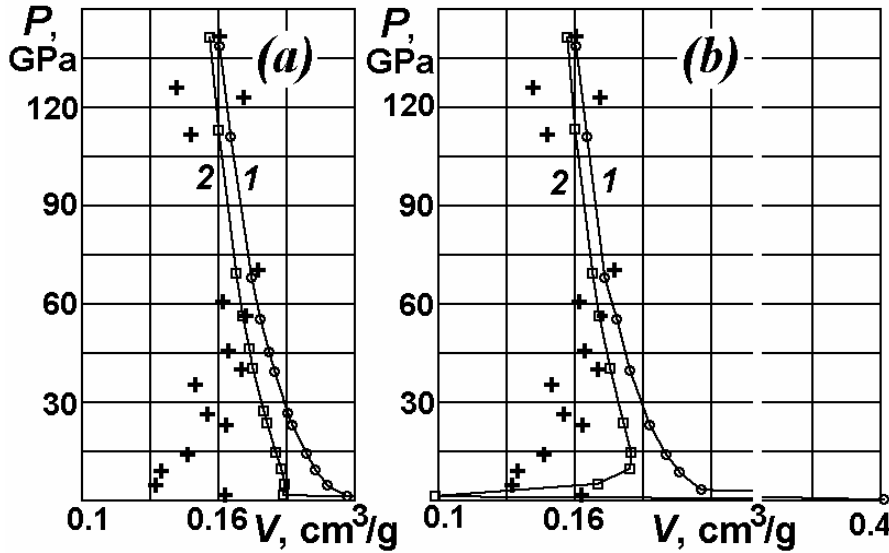


Fig. 15. The  $(P, V)$ -response curves for the case of negligible wave attenuation (a) and for the case when the shock attenuation affects the data (b)

It is interesting to note that the pressure deviations are quite small. Thus, the density obtained with the data reduction is actually the major factor contributing to the disagreement. Remarkably, curve 2 in Fig. 15(a) traces quite well the well-known quasi-static behaviour of porous material; at the same time, curve 2 in Fig. 15(b) demonstrates clear signs of the compression abnormality that is typically reported for highly porous materials. In contrast, the Hugoniot states achieved in the material behind the shock front (curves 1) are close to each other regardless of the set-up. All of the data, including the instantaneous Hugoniots (curves 1), calculated IM-reduced data Hugoniots (curves 2) and reported experimental data converge to each other as the pressure increases, when the non-equilibrium effects vanish and the jump-like feature prevails in the shock profile.

## 8. Discussion on the non-equilibrium and energy exchange kinetics

In the present Section we will try to analyse the non-equilibrium compression response in slightly more detail from the viewpoint of its influence on the Hugoniot curves.

The Hugoniot parameters for materials exhibiting constitutive behaviour could be interpreted in two ways; non-equilibrium and quasi-equilibrium. The non-equilibrium (instantaneous) Hugoniot state could be defined in the traditional way as that directly behind the main shock front (such as the F-state considered above). The quasi-equilibrium Hugoniot states could be defined as those along the shock path at any time behind the shock front and they are associated with the load application time. In the experiments [6], the observed shock velocities were stationary regardless of the sample thickness. However, it should be mentioned that

other parameters were not controlled in the experiments because the shock velocity was the only parameter measured. Therefore, if other parameters varied behind the shock front along the wave propagation path, they could not be deduced from the experimental time of arrival data. According to our modelling representations, that does not contradict the experimental results, since the non-equilibrium Hugoniot state can vary depending on how long the shock wave propagates within the material. From this viewpoint the Hugoniot state depends on the sample thickness and in order to specify it experimentally, the wave profiles must be recorded. At the same time, quasi-equilibrium Hugoniot states change slowly (compared to the transformation time in the shock wave) along the wave propagation path. The longer a wave propagates the closer the states are to the equilibrium Hugoniot.

To illustrate that the shock velocity data is not sufficient for a full description of the Hugoniot in the (P,V)-space, calculations below are conducted for the basic set-up with a modified heat exchange kinetics. The shock attenuation effects are eliminated in these calculations by appropriate selection of the flyer plate thickness. Starting from the energy conservation laws for the two phases, where a specific heat transfer coefficient  $h$  can be introduced, it is easy to associate the rate function for the parameter  $\chi$  with the heat transfer kinetic proportional to  $hT(T_1-T_2)^2/(\rho T_1 T_2 s^2)$ . In terms of the kinetic for the parameter  $\chi$ , we can choose the following non-negative function  $\omega_0$  as the kinetic function:

$$\omega_0 = \frac{hT}{\rho T_1 T_2 s^n} ,$$

where

$$n = 2.2 - 10 \ln \left[ \ln \left( \frac{T}{T_c} \right) \right] , \quad \ln (T/T_c) > 1$$

$$n = 2.0 , \quad \text{otherwise} .$$

The specific heat transfer coefficient is taken to be  $h = 10^4 \text{ W}/(\text{m}^3 \cdot \text{grad})$ ,  $T_c = 10^4 \text{ K}$ .

The calculated data for the shock and particle velocities are summarised in Fig. 16 (corresponding data for the previous calculation are shown in Figs. 13(a) and 13(c)). The (D-U)-dependence for the screen material is identical to that shown in Fig. 13(b). Details of the data are reported in the table form in Table 3. Only the aluminium-screen data points and points for porosity  $m = 4$  are reported in this case.

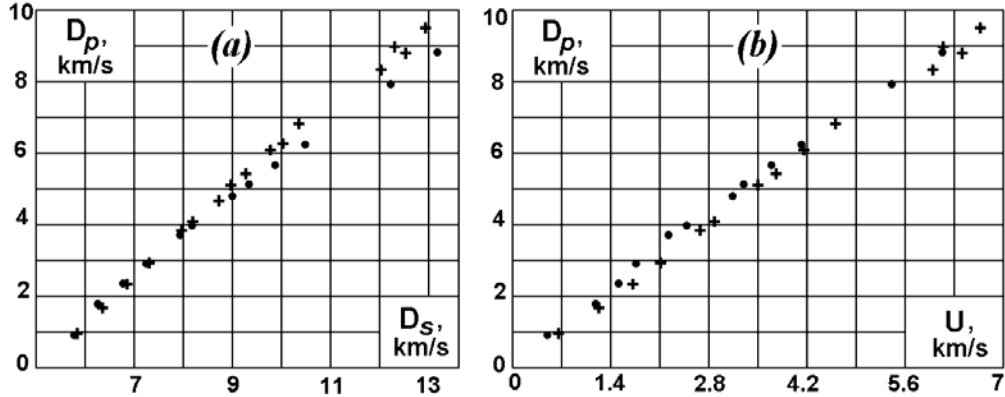


Fig. 16. The (D-D)-dependence for the basic set-up (a) and the (D-U)-dependence for the investigated material (b) with elimination of the shock attenuation effects. The calculations (solid points) are compared with the experiment (crosses).

Table 3. Results of calculation with the modified kinetics and comparison with experiment

N	Dcal	Dexp	Ucal	Uexp	$\rho$ cal	$\rho$ red
1	0.905	0.946	0.51	0.661	5.69	7.402
2	1.76	1.66	1.19	1.235	6.11	8.71
3	2.35	2.33	1.52	1.725	6.18	8.588
4	2.90	2.93	1.76	2.12	6.03	8.066
5	3.69	3.84	2.23	2.68	5.79	7.382
6	3.96	4.07	2.49	2.89	6.21	7.6916
8	4.80	5.10	3.14	3.51	6.59	7.153
9	5.13	5.41	3.31	3.77	6.67	7.356
10	5.66	6.07	3.70	4.16	6.88	7.087
12	6.24	6.81	4.13	4.61	6.96	6.903
13	7.91	8.325	5.42	6.00	7.51	8.0
16	8.82	9.51	6.13	6.68	7.77	7.4937
17	10.38	11.028	7.32	8.0	8.09	8.146

It is seen that description of experimental data is even better for this case in the low velocity region (up to 5%) when comparing with the results of the previous calculation. However, in the high-velocity range agreement of the (D-U)-results with those reported in the experimental works is actually worse than in the previous case (shown in Fig. 13(a)).

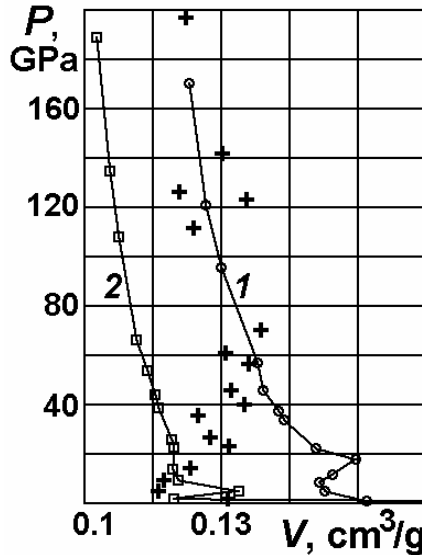


Fig. 17. The  $(P, V)$ -response curves for the case of negligible wave attenuation and modified heat transfer kinetic

It should be remembered that the particle velocity data is not obtained directly in the experiments. Overall, the calculated and experimental shock velocity dependencies ((D-D)-data) agree well for both calculations.

It is interesting to compare the Hugoniots for both cases. The Hugoniot for the previous case is shown in Fig. 15(a) and a similar plot for the present case is shown in Fig. 17, keeping the same notations. Several comments can be made concerning the calculated Hugoniot. Firstly, there is a significant pressure difference between the IM-reduced data Hugoniot (curve 2), the calculated Hugoniot (curve 1), and corresponding experimental points. This is obviously caused by significant non-equilibrium behind the shock front. It is interesting to note that the present Hugoniots demonstrate the abnormality feature for both curves in the conditions where the wave attenuation effect is eliminated.

In order to observe the non-equilibrium behaviour we draw the shock wave profiles for quite strong shock wave (velocity of the driving plate is 3 km/s). In this case for the previous calculation we observed negligible non-equilibrium effects (Figs. 11-12). In the present case we observe a strong non-equilibrium with a distinct kinetic effect at the shock front as shown in Fig. 18. Two consecutive profiles in Fig. 18 correspond to the time samples at 0.5 and 1  $\mu$ sec. Obviously, the modified kinetic uses a boosted (even for such extreme pressures and temperatures) heat transfer coefficient, activating easily the kinetic behaviour behind the shock front. Nevertheless, this calculation illustrates quite clearly that the time of arrival (shock velocity) data can be described well using different kinetics. Therefore, the shock profiles recorded in experiments would be the very useful information for description of the shock compression of materials exhibiting constitutive behaviour.

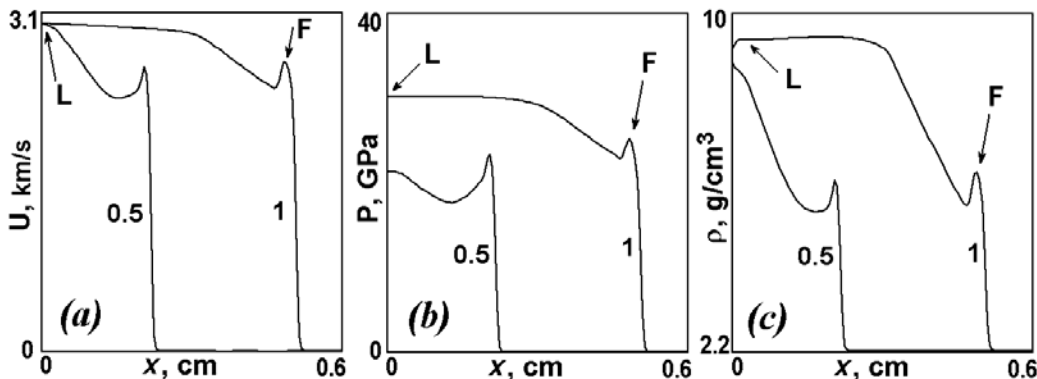


Fig. 18. The velocity (a), stress (b), and density (c) profiles for the wave at  $U_0 = 3 \text{ km/s}$

In turn, consideration of a complex thermal excitation mechanism tends to complicate the constitutive behaviour of a material and activates non-equilibrium behaviour behind the shock front. In this case several factors are influential in the Hugoniot description in the pressure-density space: 1) position of the point, where data are taken from, from the loading surface, which determines the loading duration by the first wave (precursor); 2) duration of the loading due to the main loading wave; and 3) effect of the precursor rarefaction from the free surface of the sample.

The jump-like approximation is used for argumentation [47] of the anomalous behaviour that includes:

- i) assumption of a much larger energy increase for porous material (from the energy balance equation through the jump in system (1)) due to a larger volume increment when compared with the energy increase for solid material;
- ii) use of Mie-Gruneisen equation of state for both a solid material and a porous material (mixture of gaseous and solid phases), using a single Gruneisen coefficient; and
- iii) assumption of different physical mechanisms of the material response for porous and solid substances, focusing on the activation of a high-temperature mechanism in a porous material due to the extreme energy increase; the only obvious difference between these substances is the presence of the gaseous phase, so the high-temperature mechanism can be activated only by compression of the gaseous phase.

When the jump-like approximation is critically reviewed it appears that:

- i) the energy increase might be much less than expected due to several shock transformations; firstly, pre-compacting the material by the precursor and, secondly, transforming it into the final pressure state; as a result, the energy calculated from system (1) is incremented in several steps (in a more isoentropic fashion);
- ii) the Mie-Gruneisen approximation can be valid for each of the phases. However, this approximation with a single Gruneisen coefficient might be not applicable to a mixture of the two phases, where the gaseous phase can change this coefficient significantly during the shock compression; and

- iii) while some high-temperature effects are obvious for porous materials, the effect might be overestimated. For example, data [1, 5, 6] claim that the experimental data for the porous materials in the atmospheric air environment and for samples with the air evacuated from the pores are similar. This claim does actually reduce the high-temperature contribution from compressed air in the pores, at least into the (D-D)-data.

Commenting on the first item above, as seen from data [14-16], it is hard to resolve the compression curve structure in order to find shock wave stability conditions similar to the phase transition or elastic-plastic transformations. Nevertheless, from the general assessment of the precursor velocity it is seen that at a precursor velocity of the order of 4 km/s for the porous copper (that is not in contradiction with experiments [1,6]), wave stability could be expected at the behind-shock pressures of more than 26 GPa and, correspondingly, at the behind-shock particle velocities of more than 3 km/s. This is in agreement with the compression behaviour and calculated velocities. It is remarkable, that the abnormality area is within the possible instability area, so the wave splitting/ instability, resulting in a gradual energy increments that are lower than the jump-like energy increase, might be associated with the energy overestimate.

## 9. Conclusions

Direct constitutive modelling has been used to simulate Hugoniot experiments on porous copper with a porosity  $m = 4$ . The present calculations cannot fully reproduce the conditions of the experiments because the published experimental set-ups lack the necessary details. Keeping in mind significant uncertainties in the description of experimental set-ups, parameters of the set-ups, and the procedures of data IM-reduction and elimination of the shock wave attenuation effects applied to the published experimental data, the calculations demonstrate a consistent agreement with shock velocity data obtained in the experiments.

The present work shows that a satisfactory description of the experiments can be obtained without assumptions of an abnormal behaviour of a porous material. Resistance of material to compression due to possible high-temperature expansion can easily be overestimated if the constitutive behaviour of porous material is not taken into account. The abnormality may also be associated with the wave attenuation effects and be a result of the IM-reduction procedure applied to the data, which relates the Hugoniot states to the particle velocity of material at the screen-sample interface.

Non-equilibrium behind the shock front could be an essential factor when constructing a Hugoniot in the pressure-density space. The Hugoniot is dependent on the location of a state on the shock profile where the state is taken for calculation of the Hugoniot. As a result, for the materials exhibiting distinct constitutive behaviour, the Hugoniot may depend on the sample thickness even if the shock velocity does not change essentially with the thickness. The present work has attempted to evaluate possible contributions of the constitutive behaviour to the data interpretation, which can be so significant as to appear as an abnormality.

## 10. References

1. Trunin R.F., Shock Compression of Condensed Materials, Cambridge University Press, Cambridge, UK, 1998.
2. Walsh J.M., Rice M.H., McQueen R.G., and Yarger F.L., Shock-Wave Compressions of Twenty-Seven Metals. Equations of State of Metals, *Phys. Rev.*, 108, 196-216 (1957), Issue 2 - 15 October 1957.
3. Al'tshuler L.V., Krupnikov K.K., and Brazhnik M.I., Dynamic compressibility of metals under pressures from 400,000 to 4,000,000 atmospheres, *Soviet Physics JETP*, 1958, v. 7, n. 4, pp. 614-619.
4. Al'tshuler L.V., Development of Dynamical Methods of Investigation of High Pressures in Russia, In: High-Pressure Shock Compression of Solids VII, edited by V E Fortov, L V Al'tshuler, R F Trunin, and A I Funtikov, Springer-Verlag, 2004, pp. 1-37.
5. Trunin R.F., Krupnikov K.K., Simakov G.V., and Funtikov A.I., Shock-Wave Compression of Porous Metals, In: High-Pressure Shock Compression of Solids VII, edited by V E Fortov, L V Al'tshuler, R F Trunin, and A I Funtikov, Springer-Verlag, 2004, pp. 177-195.
6. Trunin R.F., Simakov G.V., Sutulov Yu.N., Medvedev A.B., Rogozkin B.D., and Fedorov Yu.E., Compressibility of porous metals in shock waves, *Soviet Physics JETP*, 1989, v. 69, n. 3, pp. 580-588.
7. Trunin R.F., Shock compressibility of condensed materials in strong shock waves generated by underground nuclear explosions, *Physics-Uspekhi*, 1994, v. 37, n. 11, pp. 1123-1145.
8. Trunin R.F., Medvedev A.B., Funtikov A.I., Podurets M.A., Simakov G.V., and Sevast'yanov A.G., Shock compression of porous iron, copper, and tungsten, and their equation of state in the terapascal pressure range, *Soviet Physics JETP*, 1989, v. 68, n. 2, pp. 356-361.
9. Kormer S.B., Funtikov A.I., Urlin V.D., and Kolesnikova A.N., Dynamic compression of porous metals and the equation of state with variable specific heat at high temperatures, *Soviet Physics JETP*, 1962, v. 15, n. 3, pp. 477-488.
10. Zubarev V.N., Podurets M.A., Popov L.V., Simakov G.V., and Trunin R.F., Shock compressibility and equation of state for copper in a high pressure region [in Russian], In: Detonation: Critical phenomena. Physical-Chemical transformations in shock waves (F.I. Dubovitsky, ed.), Dept. of Institute of Chemical Physics, USSR Academy of Sciences, Chernogolovka, 1978, pp. 61-65.
11. Marsh S.P. (Ed.), LASL Shock Hugoniot Data, University of California Press, Berkley and Los Angeles, California, 1980.
12. van Thiel M., Shaner J., and Salinas E. (Eds.), Compendium of Shock Wave Data, Lawrence Livermore Laboratory Report UCRL-50108, University of California, Livermore, Vol. 1, 1977.
13. Bolkhovitinov L.C. and Khvostov Yu.B., Polystyrene and copper isentropes obtained on the data of shock compressed materials of high porosity, *Lett. Appl. Engng. Sci.*, 1984, v. 22, n. 4, pp. 491-504.
14. Boade R.R., Compression of Porous Copper by Shock Waves, *J. Appl. Physics*, 1968, v. 39, n. 12, pp. 5693-5702.

15. Boade R.R., Principle Hugoniot, Second-Shock Hugoniot, and Release Behavior, of Pressed Copper Powder, *J. Appl. Physics*, 1970, v. 41, n. 11, pp. 4542-4551.
16. Linde R.K., Seaman L., and Schmidt D.N., Shock response of porous copper, iron, tungsten, and polyurethane, *J. Appl. Physics*, 1972, v. 43, n. 8, pp. 3367-3375.
17. Trunin R.F., Podurets M.A., Moiseev B.N., Simakov G.V., and Popov L.V., Relative compressibility of copper, cadmium and lead at high pressures, *Soviet Physics JETP*, 1969, v. 29, n. 4, pp. 630-631.
18. Alekseev Yu.L., Ratnikov V.P., and Rybakov A.P., Shock adiabats of porous metals, *J. Appl. Mech. Techn. Physics*, 1971, v. 12, n. 2, pp. 257-262.
19. Bakanova A.A., Dudoladov I.P., and Sutulov Yu.N., Shock compressibility of porous tungsten, molybdenum, copper, and aluminium in the low pressure domain, *J. Appl. Mech. Techn. Physics*, 1974, v. 15, n. 2, pp. 241-245.
20. Al'tshuler L.V., Bushman A.V., Zhernokletov M.V., Zubarev V.N., Leont'ev A.A., and Fortov V.E., Unloading isentropes and the equation of state of metals at high energy densities, *Soviet Physics JETP*, 1980, v. 51, n. 2, pp. 373-383.
21. Gryaznov V.K., Fortov V.E., Zhernokletov M.V., Simakov G.V., Trunin R.F., Trusov L.I., and Iosilevskii I.L., Shock compression and thermodynamics of highly nonideal metallic plasma, *Soviet Physics JETP*, 1998, v. 87, n. 4, pp. 678-690.
22. Nellis W.J., Moriarty J.A., Mitchell A.C., Ross M., Dandrea R.G., Ashcroft N.W., Holmes N.C., and Gathers G.R., Metals Physics at Ultrahigh Pressure: Aluminum, Copper, and Lead as Prototypes, *Phys. Rev. Lett.*, 1988, v. 60, n. 14, pp. 1414-1417.
23. Butcher B. M., Carroll M. M., and Holt A.C., Shock-wave compaction of porous aluminum, *J. Appl. Phys.*, v. 45, n. 9, 1974, pp. 3864-3875.
24. Resnyansky A.D. and Bourne N.K., Shock-wave compression of a porous material, *J. Appl. Physics*, 2004, v. 95, n. 4, pp. 1760-1769.
25. Trunin R.F., Shock compression of condensed materials (laboratory studies), *Physics-Uspekhi*, 2001, v. 44, n. 4, pp. 371-396.
26. Al'tshuler L.V., Trunin R.F., Krupnikov K.K., and Panov N.V., Explosive laboratory devices for shock wave compression studies, *Physics-Uspekhi*, 1996, v. 39, n. 5, pp. 539-544.
27. Al'tshuler L.V., Trunin R.F., Urlin V.D., Fortov V.E., and Funtikov A.I., Development of dynamic high-pressure techniques in Russia, *Physics-Uspekhi*, 1999, v. 42, n. 3, pp. 261-280.
28. Asay J.R., Shock wave paradigms and new challenges, In: *Shock Compression of Condensed Matter - 2001*, edited by M D Furnish, N N Thadhani, and Y Horie, (AIP, New York, 2002), CP620, 2002, pp. 26-35.
29. Mallory H.D., Propagation of Shock Waves in Aluminum, *J Appl. Physics*, 1955, v. 26, n. 5, pp. 555-559.
30. Goranson R.W., Bancroft D., Burton B.L., Blechar T., Houston E.E., Gittings E.F., and Landeen S.A., Dynamic Determination of the Compressibility of Metals, *J Appl. Physics*, 1955, v. 26, n. 12, pp. 1472-1479.
31. Bugaeva V.A., Evtigneev A.A., and Trunin R.F., Analysis of Calculation Data on the Adiabats of Expansion for Copper, Iron, and Aluminium, *High Temperature*, 1996, v. 34, n. 5, pp. 674-680.
32. Avrorin E.N., Vodolaga B.K., Simonenko V.A., and Fortov V.E., Intense shock waves and extreme states of matter, *Physics-Uspekhi*, 1993, v. 36, n. 5, pp. 337-364.

33. Grady D.E., Hydrodynamic compressibility of silicon carbide through shock compression of metal-ceramic mixtures, *J Appl. Physics*, 1994, v. 75, n. 1, pp. 197-202.
34. Grady D., Analytical solutions and constitutive relations for shock propagation in porous media, In: *Shock Compression of Condensed Matter - 2003*, edited by M D Furnish, Y M Gupta, and J W Forbes, (AIP, New York, 2004), CP706, 2004, pp. 205-208.
35. Resnyansky A.D. and Bourne N.K., Shock compression of dry and hydrated sand, In: *Shock Compression of Condensed Matter - 2003*, edited by M D Furnish, Y M Gupta, and J W Forbes, (AIP, New York, 2004), CP706, 2004, pp. 1474-1477.
36. Carroll M.M. and Holt A.C., Static and Dynamic Pore-Collapse Relations for Ductile Porous Materials, *J Appl. Physics*, 1972, v. 43, n. 4, pp. 1626-1636.
37. Kapila A.K., Menikoff R., Bdzil J.B., Son S.F., and Stewart D.S., Two-phase modeling of deflagration-to-detonation transition in granular materials: Reduced equations, *Physics of Fluids*, 2001, v. 13, n. 10, pp. 3002-3024.
38. Godunov S.K., Kozin N.S., and Romenskii E.I., Equations of state of the elastic energy of metals in the case of a nonspherical strain tensor, *J. Appl. Mech. and Techn. Phys.*, 1974, v. 15, n. 2, pp. 246-250.
39. Resnyansky A.D. and Romensky E.I., Numerical Modelling the Non-Equilibrium Phase Transitions in the Continuum Media By a Nonlinear Kinetics, *DYMAT Journal*, 1995, v. 2, n. 3/4, pp. 223-228.
40. Godunov S.K., Zabrodin A.V., Ivanov M.Ya., Kraiko A.N., and Prokopov G.P., *Numerical Solution of Multi-Dimensional Problems of Gas Dynamics*, Nauka Press, Moscow, 1976 (French transl: *Résolution Numérique des Problèmes Multidimensionnels de la Dynamique des Gaz*, Mir, Moscow, 1979).
41. Resnyansky A.D., A technique of use of arbitrary equations of state in the Riemann problem for the Godunov scheme [in Russian], *Dynamics of Continua (Dinamika sploshnoi sredy)*, Lavrentyev Institute of Hydrodynamics, Novosibirsk, USSR, 1988, n. 86, pp. 88-95.
42. Godunov S.K. and Romenskii E.I., "Elements of Continuum Mechanics and Conservation Laws", Kluwer Academic Publ., N.Y., 2003.
43. Resnyansky A.D., DYNA-modelling of the high-velocity impact problems with a split-element algorithm, *Int. J. Impact Eng.*, 2002, v. 27, n. 7, pp. 709-727.
44. Trunin R.F. and Panov N.V., Shock Compression of Porous Copper at Megabar Pressures, *High Temperature*, 2000, v. 38, n. 5, pp. 754-758.
45. Lindholm U.S. and Yeakley L.M., High Strain-rate Testing: Tension and Compression, 1968, *Exp. Mech.*, v. 8, pp. 1-9.
46. Heyda J.F., Plate-gap model of a porous solid and its application to impact by reduced density projectiles, NASA report NASA CR-1140, NASA-Langley, 1968.
47. Zel'dovich Ya. B. and Raizer Yu. P., "Physics of shock waves and high-temperature hydrodynamic phenomena", vol. 2, Academic Press, N.Y., 1967.
48. Godunov S.K., Zabrodin A.V., Ivanov M.Y., Kraiko A.N., Prokopov G.P., "Résolution numérique des problèmes multidimensionnels de la dynamique des gaz", Mir, Moscow, 1979 [in French, transl. from "Numerical solution of multi-dimensional problems in gas dynamics", Nauka Press, Moscow, 1976, in Russian].
49. Kolgan V.P., Application of the minimum-derivative principle in the construction of finite-difference schemes for numerical analysis of discontinuous solutions in gas dynamics [in Russian], *Uch. Zap. TsaGI*, 1972, v. 3, n. 6, pp. 68-77.



## Appendix A: Nonlinear Riemann problem for arbitrary equation of state

This Appendix describes briefly the method of calculation of the Riemann problem for an isotropic material with an arbitrary two-parameter Equation Of State (EOS); the method is applicable to the Godunov scheme with the second order spatial accuracy. This method has been used for a variety of two-phase materials and the mathematical rationale of the method has been published earlier in [41]. The method allows one to approximate an arbitrary EOS as an extension of the ideal gas EOS in the following form:

$$p = A(S) \left( \frac{\rho}{\rho_0} \right)^\gamma - p^0, \quad (19)$$

we require here fulfilment of the condition  $A' > 0$ . Suppose we have an arbitrary EOS in the following form

$$\tilde{p} = f(\rho, S) \quad , \quad (20)$$

where the function  $f$  obeys the following conditions of normal material:  $f_\rho > 0$  and  $f_{\rho\rho} > 0$ . For the Riemann problem with initial parameters  $p_1, \rho_1, u_1$  and  $p_2, \rho_2, u_2$  on the left and right from a contact surface of a 'shock tube' (we denote the materials with such the initial states as materials '1' and '2') we need to find a solution at the contact surface at  $t > 0$ . It should be noted that from the EOS (20) the parameters  $S_1$  and  $S_2$  at  $t = 0$  can be found as well. Exact solutions of the Riemann problem for the Godunov scheme are documented well [48] for the EOS in the form (19) even if the constants  $p_0$  and  $\gamma$  are different in the materials '1' and '2'. In the present work, the Godunov scheme [48] is used in the second order accuracy modification published in [49].

Now for the materials '1' and '2' we can introduce the following constants associated with the current states  $(p_1, \rho_1, S_1)$  and  $(p_2, \rho_2, S_2)$ :

$$\begin{aligned} \gamma_1 &= 1 + \frac{\rho_1 \tilde{p}_{\rho\rho}(\rho_1, S_1)}{\tilde{p}_\rho(\rho_1, S_1)}, & p_1^0 &= \frac{\rho_1 \tilde{p}_\rho(\rho_1, S_1)}{\gamma_1} - \tilde{p}(\rho_1, S_1), \\ \gamma_2 &= 1 + \frac{\rho_2 \tilde{p}_{\rho\rho}(\rho_2, S_2)}{\tilde{p}_\rho(\rho_2, S_2)}, & p_2^0 &= \frac{\rho_2 \tilde{p}_\rho(\rho_2, S_2)}{\gamma_2} - \tilde{p}(\rho_2, S_2). \end{aligned}$$

Then, we can use the EOS (19) with the constants  $\gamma_1$  and  $p_1^0$  instead of  $\gamma$  and  $p^0$  for the material '1' and the same EOS with the constants  $\gamma_2$  and  $p_2^0$  for the material '2'. It has been proved in the publication [41] that solution of the Riemann problem using these EOSs approximates with second order accuracy the solution of the Riemann problem using the EOS (20).



## Appendix B: Impedance mismatch procedure

This Appendix describes the procedure of calculation of the shock Hugoniot parameters using the Impedance Mismatch (IM) method and evaluates possible errors for the parameters due to errors in the shock velocity determination. Assuming the jump-like approximation for the shock wave and using the standard assumptions for a Hugoniot [3], we relate the shock velocity to the particle velocities in the standard material via a linear dependence:

$$D_s = a + b \cdot U . \quad (21)$$

Referring to the schematic in Fig. 2(b), the Hugoniot  $H_s$  is approximated as the following quadratic dependence

$$P = \rho_0 U \cdot (a + b \cdot U) , \quad (22)$$

when neglecting the initial pressure and particle velocity in front of the shock. Then, in agreement with [3], we approximate the rarefaction curve  $R_s$  by the mirrored Hugoniot  $H_s^-$  with respect to the impact velocity  $2U_0$  that is expressed by the following equation

$$P = -\rho_f (U - 2U_0) \cdot (a - b \cdot (U - 2U_0)) . \quad (23)$$

It should be noted that the particle velocity in the screen  $U_0$  can be found from the Hugoniot relation (21) if the shock velocity  $D_s$  in the standard has been recorded in the experiment. When the shock velocity  $D$  ( $D_p$  in Fig. 2) in the investigated material has also been measured, the particle velocity  $U_h$  at point 2 in Fig. 2(b) can be calculated from the intersection of the Hugoniot  $H_s^-$  defined by equation (23) with the Rayleigh line  $P = \rho_{00} \cdot U \cdot D$ . This gives

$$U_h = 2U_0 + \left[ \rho_s a + \rho_{00} D - \sqrt{(\rho_s a + \rho_{00} D)^2 + 8\rho_s b \rho_{00} D U_0} \right] / (2\rho_s b) . \quad (24)$$

Suppose we have tabulated the (D-U)-Hugoniot (21) of the standard with very good accuracy so that we can neglect inaccuracies in determination of the curve. Thus, we can also neglect inaccuracies in  $U_0$  that is calculated from (21) and appears in (24).

Let us evaluate the possible error for the velocity  $U_h$  if an  $100 \times \delta\%$  error has been made in the determination of the shock velocity  $D$ . Denote the erroneous shock velocity by  $D'$  so that

$$D' - D = \delta \cdot D \quad (25)$$

Then, the corresponding particle velocity  $U_h'$  is obtained from (24) with  $D$  replaced by  $D'$ . Subtracting  $U_h'$  from  $U_h$  (obtained from (24)), the error estimate for  $U_h$  can be found as follows

$$\frac{U_h' - U_h}{U_h} = \frac{D' - D}{KD} , \quad K = \frac{\sqrt{(\rho_f a + \rho_{00} D)^2 + 8\rho_f b \rho_{00} D U_0}}{\rho_{00} D} . \quad (26)$$

Assuming that the Hugoniot  $H_s$  is built up without errors and the locus of the rarefaction states in Fig. 2 follows the curve  $H_s^-$ , it is seen that  $K > 1$  and the error in  $U_h$  is of the same order as the error in  $D$ . Thus, from (25) and (26) an error for the disturbed particle velocity is  $U_h' - U_h = \delta \cdot U_h / K$ . Thus, the error in the particle velocity is  $K$  times less than the error in the shock velocity, and the  $K$ -coefficient depends mainly on the initial parameters, the Hugoniot of the standard material and the magnitude of the wave propagating in the standard and test materials ( $U_0$  and  $D$ ). For the aluminium standard and the porous material analysed this coefficient varies from 10 at a low velocity of impact down to 3 at the highest impact velocity from the load range analysed. It should be noted that this is an upper estimate of the error because at the high velocity of impact the mirror approximation of  $R_s$  by  $H_s^-$  deteriorates and at the low velocity of impact the precursor multiple reflection and circulation effects interfere with the approximation. However, the  $U_h$ -error is at least not larger than the  $D$ -error. The pressure error, in the first order, is

$$P' - P = \rho_{00}(D'U_h' - DU_h) \approx \delta \cdot P \cdot (1 + 1/K) . \quad (27)$$

Thus, the  $P$ -error can be slightly greater than the  $D$ -error although of similar magnitude. The last parameter we estimate is error in determination of density. Evaluating density from  $\rho_{00}/\rho = (D - U_h)/D$ , we have

$$\frac{\rho_{00}}{\rho'} - \frac{\rho_{00}}{\rho} = \frac{U_h}{D} - \frac{U_h'}{D'} \approx K_r \delta , \quad K_r = \frac{U_h}{D} \left( 1 + \frac{1}{K} \right) . \quad (28)$$

For the porous copper  $D \sim 1.5U_h$  and, thus, the coefficient  $K_r$  is of the order of 1 (more precisely, between 0.75 and 1, neglecting the non-equilibrium and the mirror Hugoniot issues). When calculating density, we have

$$\frac{\rho - \rho'}{\rho} \approx \frac{\rho}{\rho_{00}} \cdot K_r \delta . \quad (29)$$

This means that at compression of a porous material when the density approaches the density of the solid phase  $\rho_0$ , the  $\rho$ -error may be as high as  $mK_r\delta$  ( $m = \rho_0/\rho_{00}$ ). For the porous copper considered above  $m = 4$  and the error varies between  $3\delta$  and  $4\delta$ , thus, exceeding the  $D$ -error by a factor of 3-4.

DEFENCE SCIENCE AND TECHNOLOGY ORGANISATION DOCUMENT CONTROL DATA		1. PRIVACY MARKING/CAVEAT (OF DOCUMENT)		
<p>2. TITLE</p> <p>Constitutive Modelling of the Shock Behaviour of a Highly Porous Material</p>		<p>3. SECURITY CLASSIFICATION (FOR UNCLASSIFIED REPORTS THAT ARE LIMITED RELEASE USE (L) NEXT TO DOCUMENT CLASSIFICATION)</p> <p>Document (U) Title (U) Abstract (U)</p>		
<p>4. AUTHOR(S)</p> <p>A. D. Resnyansky</p>		<p>5. CORPORATE AUTHOR</p> <p>DSTO Defence Science and Technology Organisation PO Box 1500 Edinburgh South Australia 5111 Australia</p>		
6a. DSTO NUMBER DSTO-TR-2026	6b. AR NUMBER AR-013-957	6c. TYPE OF REPORT Technical Report	7. DOCUMENT DATE July 2007	
8. FILE NUMBER 2007/ 1053740/1	9. TASK NUMBER LRR05/299	10. TASK SPONSOR DSTO	11. NO. OF PAGES 38	12. NO. OF REFERENCES 49
<p>13. URL on the World Wide Web <a href="http://www.dsto.defence.gov.au/corporate/reports/DSTO-TR-2026.pdf">http://www.dsto.defence.gov.au/corporate/reports/DSTO-TR-2026.pdf</a></p>		<p>14. RELEASE AUTHORITY Chief, Weapons Systems Division</p>		
<p>15. SECONDARY RELEASE STATEMENT OF THIS DOCUMENT</p> <p><i>Approved for public release</i></p> <p>OVERSEAS ENQUIRIES OUTSIDE STATED LIMITATIONS SHOULD BE REFERRED THROUGH DOCUMENT EXCHANGE, PO BOX 1500, EDINBURGH, SA 5111</p>				
<p>16. DELIBERATE ANNOUNCEMENT No Limitations</p>				
<p>17. CITATION IN OTHER DOCUMENTS Yes</p>				
<p>18. DSTO RESEARCH LIBRARY THESAURUS</p> <p>Shock Physics Porous Materials Constitutive Modelling Two-phase Model Non-equilibrium Behaviour</p>				
<p>19. ABSTRACT</p> <p>The report studies the constitutive behaviour of highly porous materials. This study is driven by efforts for the development and validation of a multi-phase modelling capability in DSTO, which aims at an enhanced evaluation of blast mitigation by porous materials. A two-phase model is employed for the description of a porous material, for which experimental shock velocity data are widely available in literature. The method deriving Hugoniots from the shock velocity data is critically approached. The importance of the non-equilibrium behaviour analysis is demonstrated, and it is shown that the stress or velocity profiles need to be considered, using relevant experiments and constitutive modelling. It is argued that the apparent anomalous behaviour of the Hugoniots of a highly porous material might be caused by misinterpretation of the experimental data.</p>				